TRANSPORT AND DEPOSITION OF MUD IN DEEP-WATER ENVIRONMENTS: PROCESSES AND STRATIGRAPHIC IMPLICATIONS

KÉVIN BOULESTEIX*, MIQUEL POYATOS-MORÉ†, STEPHEN S. FLINT*, KEVIN G. TAYLOR*, DAVID M. HODGSON‡ and STEPHEN T. HASIOTIS§

*School of Earth and Environmental Sciences, University of Manchester, Manchester M13 9PL, UK (E-mail: kevin.boulesteix@gmail.com)

†Department of Geosciences, University of Oslo, Oslo 0371, Norway

‡School of Earth and Environment, University of Leeds, Leeds LS2 9JT, UK

§Department of Geology, University of Kansas, Lawrence, Kansas 66045-7575, USA

Associate Editor – Kyle Straub

Short title – Deep-water mud transport and deposition

ABSTRACT

Deep-water mudstones are often considered as background sediments, deposited by vertical suspension fallout, and the range of transport and depositional processes are poorly understood compared to their shallow-marine counterparts. Here, we present a dataset from a 538.50 m-thick cored succession through the Permian muddy lower Ecca Group of the Tanqua depocentre (southwest Karoo Basin, South Africa). This study aims to characterize the range of mudstone facies, transport and depositional processes, and stacking patterns recorded in deep-water environments prior to deposition of the Tanqua Karoo sandy basin-floor fans. A combination of macroscopic and microscopic description techniques and ichnological analysis has defined nine sedimentary facies that stack in a repeated pattern to produce 2–26-m-thick depositional units. The lower part of each unit is characterized by

bedded mudstone deposited by dilute, low-density turbidity currents with evidence for hyperpycnal-flow processes and sediment remobilization. The upper part of each unit is dominated by more organic-rich bedded mudstone with common mudstone intraclasts, deposited by debris flows and transitional flows, with scarce indicators of suspension fallout. The intensity of bioturbation and burrow size increases upward through each depositional unit, consistent with a decrease in physicochemically stressed conditions, linked to a lower sediment accumulation rate. This vertical facies transition in the single well dataset can be interpreted to represent relative sea level variations, where the hyperpycnal stressed conditions in the lower part of the units were driven by sea level fall and the more bioturbated upper part of the unit represents backstepping, related to sea level rise. Alternatively, this facies transition may represent autogenic compensational stacking. The prevalence of sediment density flow deposits, even in positions distal or lateral to the sediment entry point, challenges the idea that deep-water mudstones are primarily the deposits of passive rainout along continental margins.

Keywords: Deep-water, depositional processes, Karoo Basin, mudstone, Permian, trace fossils, turbidite.

INTRODUCTION

Most sedimentological studies of mudstones—here defined as sedimentary rocks in which more than 50% of the grains are <62.5 µm (i.e. clay-size and silt-size particles; sensu Lazar et al., 2015)—have focused on successions deposited in shelf environments (e.g. Schieber, 1994; Macquaker and Taylor, 1996; Plint et al., 2012; Bohacs et al., 2014; Plint, 2014; Harazim and McIlroy, 2015; Wilson and Schieber, 2015; Birgenheier et al., 2017). These studies have improved current knowledge of the range of physical and biological processes responsible for the transport and accumulation of mud in shallow-water environments. In these systems, wave action has a major influence and may resuspend previously deposited mud particles to generate or enhance turbidity currents (Ichaso and Dalrymple, 2009; Macquaker et al., 2010). Recent flume experiments have demonstrated that flocculated mud can be transported as bedload at flow velocities that normally transport sand (Schieber et al., 2007; Schieber and Southard, 2009). Common aggregate grains (rip-up intraclasts, lithoclasts) in shallow-water

mudstones suggests intermittent sea floor reworking (Schieber, 1998, 1999; Schieber et al., 2010; Plint et al., 2012; Egenhoff and Fishman, 2013; Plint and Macquaker, 2013; Plint, 2014; Schieber, 2016; Li and Schieber, 2018). These observations demonstrate that mud can be transported and deposited in continental shelves by depositional processes as energetic as those for coarse-grained sediments.

Deep-water (i.e. below storm wave base) sedimentology has expanded rapidly because of the exploration and exploitation of hydrocarbons in sandy basin-floor fans and slope-channel complexes (e.g. Pettingill and Weimer, 2002; Shanmugam, 2006; Weimer et al., 2007). The focus, however, has mainly been on sandstones, whereas mudstone packages are usually described as background sedimentation, deposited by pelagic or hemipelagic vertical suspension fallout in low-energy environments with occasional turbidity currents (e.g. Scholle, 1971; Wynn et al., 2000; Southern et al., 2017; Pierce et al., 2018). This interpretation is mainly due to the generally poor exposure of mudstones at outcrop that usually precludes observation and interpretation of primary sedimentary structures and bed contacts at macroscopic scale. In sub-surface datasets, deep-water mudstones are rarely cored compared to deep-water sandstones, and where they are, they usually display a homogenous texture to the naked eye. Older studies focusing on deep-water mudstones (e.g. Stow and Shanmugam, 1980; Stow and Piper, 1984; Pickering et al., 1986) usually lack microscopic descriptions that are essential to fully characterize mudstone fabrics. More recent studies using a combination of macroscopic and microscopic description techniques have highlighted that a wide range of processes (i.e. turbidity currents, debris flows, transitional flows, mass-wasting processes) may be responsible for the transport and deposition of mud in deep-water environments (e.g. Schieber, 1999; Loucks and Ruppel, 2007; Trabucho-Alexandre, 2012; Konitzer et al., 2014; Knapp et al., 2017; Ayranci et al., 2018a; Newport et al., 2018). These findings have started to challenge the traditional view that suspension fallout is the dominant depositional process in deep-water mudstones, with major implications for the estimation of depositional rates and the correct interpretation of times of clastic starvation in deep-water environments. However, there remains a lack of detailed process-based studies focusing on long and continuous deep-water mudstone successions, that are essential to evaluate the long-term variability in depositional conditions within deep-water muddy environments.

This integrated study documents a deep-water mudstone succession using a continuous 538.50 m core section from the Lower Ecca Group of the Karoo Basin (South Africa) deposited during the

Permian icehouse-to-greenhouse transition. By combining macrofacies and microfacies descriptions, the main objectives of this study are to: (i) describe and interpret the range of facies, depositional processes, stacking patterns and trace fossils in a mudstone succession deposited in deep-water environment; (ii) document and discuss the resulting deposits of deep-water sediment density flows in the absence of sand; and (iii) discuss the controls on the stacking pattern of deep-water mudstones.

GEOLOGICAL SETTING

The Karoo Basin has been interpreted as a retro-arc foreland basin developed behind a fold-thrust belt (Cape Fold Belt) (De Wit and Ransome, 1992; Veevers et al., 1994; Visser and Praekelt, 1996; Catuneanu et al., 1998; López-Gamundi and Rossello, 1998; Viglietti et al., 2018). An alternative hypothesis is that subsidence during the deep-water phase of deposition was controlled by dynamic topography associated with the subduction of the palaeo-Pacific plate beneath Gondwana (Pysklywec and Mitrovica, 1999; Tankard et al., 2009). Mantle flow might have triggered movements along inherited basement structures that led to the development of the Tanqua and Laingsburg depocentres in the southwest Karoo Basin (Fig. 1A and B). This interpretation is consistent with provenance studies (Andersson and Worden, 2004; Van Lente, 2004) and radiometric dating (Blewett and Phillips, 2016), which indicate that the Cape Fold Belt was not emergent nor an important source of sediment for the Karoo Basin before the Triassic.

The basin fill comprises the 5500 m-thick Karoo Supergroup, deposited from Late Carboniferous to Early Jurassic (Fig. 1C) (Smith, 1990; Veevers et al., 1994). The Karoo Supergroup is composed of the glaciogenic Dwyka Group (Late Carboniferous-Early Permian), the deep-marine to shallow-marine Ecca Group (Permian) and the fluvial Beaufort Group (Permo–Triassic). The Dwyka Group is composed of four deglaciation sequences of basal diamictites overlain by rhythmites grading into mudstones (Theron and Blignault, 1975; Visser, 1997). The uppermost sequence grades into the Ecca Group, deposited approximately between 290 to 265 Ma (Belica et al., 2017). The transition from the Dwyka to Ecca Group was interpreted to mark the end of glaciations in the Karoo Basin (Bangert et al., 1999; Isbell et al., 2008).

This study focuses on the mudstone-dominated lower Ecca Group of the Tanqua depocentre,

111 which comprises the Prince Albert, Whitehill, Collingham and Tierberg formations (Fig. 1C) (Johnson et
112 al., 2006). These formations were previously interpreted as deposited in a relatively sediment-starved,
113 basin-floor environment (Visser, 1992, 1994; Viljoen, 2005), although water palaeodepth has not been
114 defined due to the absence of diagnostic microfossils. Some authors have suggested a northern source
115 for the Prince Albert, Whitehill and Collingham formations based on facies distribution and sparse
116 palaeocurrent indicators (Chukwuma and Bordy, 2016) and palynology (Götz et al., 2018). Ash beds
117 potentially derived from the Choiyoi volcanic province (Northern Patagonia) are interbedded in these
118 formations, with a higher density in the Collingham Formation (McLachlan and Jonker, 1990; Veevers
119 et al., 1994; Viljoen, 1994; McKay et al., 2015). These mudstone-rich formations are overlain by the
120 well-studied, sandy basin-floor fans of the Skoorsteenberg Formation (Wickens, 1994; Johnson et al.,
121 2001; Hodgson et al., 2006) and the upper slope to shelf deposits of the Waterford Formation (Wild et
122 al., 2009; Dixon et al., 2012; Poyatos-Moré et al., 2016; Gomis-Cartesio et al., 2016, 2018) (Fig. 1C).

123 Some authors have proposed that the Ecca Group was deposited in an open marine basin with
124 normal salinity based on the presence of marine fossils (McLachlan and Anderson, 1973; Visser, 1992;
125 Götz et al., 2018). Fully marine conditions are also suggested by Rb/K palaeosalinity proxy (Scheffler et
126 al., 2006; Geel et al., 2013). Others authors have suggested that the Ecca Group was deposited in a
127 freshwater to brackish basin with intermittent connections with the open marine environment, based on
128 ichnology (Buatois et al., 2010) and stable isotope data (Faure and Cole, 1999; Herbert and Compton,
129 2007). A multi-proxy approach combining geochemistry, palynology, and mineralogy suggests a climatic
130 transition from a cold-arid climate during deposition of the Dwyka Group to a warm-humid climate for
131 the Ecca Group (Scheffler et al., 2003, 2006).

132

133 # MATERIALS AND METHODS

134 This study is based on a 948.50-m-thick continuous core from the vertical OR-01 research borehole
135 drilled in the Tanqua depocentre (Fig. 1B). For the purpose of this paper, we focused on the lower
136 538.50-m-thick, mudstone-dominated succession (from 948.50 m up to 410 m), that includes the Prince
137 Albert, Whitehill, Collingham and Tierberg formations (Fig. 1C).

138 A sedimentary log of the core was established through wet and dry observations to record

macroscopically visible features including: (i) lithology, (ii) colour, (iii) physical sedimentary structures, (iv) bed contacts, (v) bed thicknesses, (vi) deformation, (vii) trace fossils and (viii) bioturbation index. The bioturbation index (BI) of Taylor and Goldring (1993) was used macroscopically and semi-quantitatively to describe bioturbation intensity on a 0 to 6 scale where 0 corresponds to non-bioturbated material and 6 corresponds to completely bioturbated. The presence of calcium carbonate was assessed by placing 10% hydrochloric acid directly onto the core. High-resolution photographs of the different facies and features of interest were taken using a high-resolution Nikon AF-S Micro Nikkor 60 mm F-2.8 lens (Nikon, Tokyo, Japan). Enhanced contrast images of the core using Microsoft Office Picture Manager® captured subtle colour changes and bed contacts. A total of 124 samples were collected using an adjusted uniform sampling spacing method of one sample per 5 m to include all facies and significant features of interest (i.e. stratigraphic surfaces, concretionary horizons, facies contacts, trace fossils).

A total of 27 samples were selected to represent the range of facies described from the core. Oriented polished thin sections (24×46mm) were prepared normal to bedding at 20 to 25 µm thickness to improve textural information. Thin sections were scanned using an Epson Perfection V600 photo scanner at 3200 dpi resolution (Epson, Suwa, Japan). Microscopic descriptions were done using an optical Nikon Eclipse LV100NPOL microscope fitted with a Nikon DS-Fi2 camera (Nikon, Tokyo, Japan). Grain sizes were refined from the core observations using visual estimate. Mudstones were classified into different facies based on the combination of macroscopic and microscopic descriptions. Mudstones consisting of more than half of grains <10 µm are defined as fine mudstone and those with more than half of grains 10 to 62.5 µm as coarse mudstone (McCave et al., 1995). Following the guidelines of Lazar et al. (2015), a composition modifier (e.g., siliceous, calcareous, argillaceous and carbonaceous) is added depending on the dominant grain type (quartz, carbonate, clay and organic matter, respectively). Trends in burrow size, ichnodiversity and bioturbation intensity are used qualitatively to infer sea floor physicochemical conditions (i.e. oxygen level, type of medium, salinity, sediment accumulation rate and frequency of flow events) (e.g. Bromley, 1996; MacEachern et al., 2007).

Following optical microscope descriptions, thin sections were carbon coated for electron microscope analysis. High-resolution imaging and compositional analysis were done on 5 samples using a FEI XL30 environmental scanning electron microscope (ESEM) (FEI, Hillsboro, OR, USA) with a

backscattered electron detector attached at 15 kV and a working distance of ca 10 mm.

Total organic carbon (TOC) was determined in 42 samples in a targeted part of the core (from 649.20 m up to 624.95 m) using a LECO SC-144DR (LECO Corp., St. Joseph, MI, USA) to evaluate the vertical evolution of organic enrichment. Samples were powdered using a mortar and pestle. Empty sample tubes used for analysis were weighted (m_{tube}). 0.8 g (+/- 10 %) of sediment per sample was added to the tubes. The tubes with sediment were weighted ($m_{initial}$). Samples were then prepared for total organic carbon analysis by adding 10 % HCL to remove any carbonate content. They were rinsed using distilled water and a centrifuge and dried in an oven at 60℃ overnight . The tubes with sediment were weighted after drying (m_{final}). 0.3 g of acid-washed sediment per samples was placed into the LECO to obtain the percentage carbon (P_{OC}). Total organic carbon (TOC) in the samples after carbonate removal was calculated using the formula:

$$TOC = P_{OC} \times ((m_{final} - m_{tube}) / (m_{initial} - m_{tube})). \quad (1)$$

RESULTS

Facies and depositional processes

Nine facies (F1 to F9) were determined from the combination of macroscopic and microscopic characteristics. Facies-stacking pattern is presented in Fig. 2. Facies are described below, illustrated at similar scales in Figure 3 and additional data are presented in Figs 4 to 8. The range of trace fossils is illustrated in Fig. 9. Around 90% of the succession (490 m of a total of 538.50 m) consists of coarse mudstone, whereas ~10 % consist of fine mudstone (Fig. 2). These results, however, are based on visual estimates from thin sections and continuous grain size analysis may indicate a more heterogeneous pattern. Mineralogy consists mainly of quartz and clay with subordinate feldspar, mica and wood fragments.

Facies 1: very thin-bedded mudstone

Description.

Facies 1 (F1) consists of light grey to mid-grey, continuous, siliceous-argillaceous, fine- to coarse-grained bedded mudstone (Figs 3A to C and 4A). Beds are 0.1 to 2 cm thick but usually less than 1 cm thick. Two bed types with a tripartite organization are recognized (Fig. 5). Bed type I is most common and characterized by a sharp and erosional base (Figs 4D and 5). The lower subdivision consists of structureless or continuous to discontinuous, planar-parallel to low-angle, laminated coarse mudstone. The middle subdivision is structureless and consists of normally graded to ungraded coarse mudstone. The upper subdivision consists of mottled, fine mudstone. A grain-size break is common between the middle and upper subdivisions but some beds show a conformable upper subdivision. Bed type II is characterized by a sharp and erosional or gradational base (Figs 4E and 5). The lower subdivision consists of inversely graded, planar-parallel laminated, fine to coarse mudstone. The middle and upper subdivisions are similar to bed type I. Some beds are truncated by the overlying bed (Fig. 5). Rare small-scale scours are observed (Fig. 4B). Post-depositional features include soft-sediment deformation (convolute laminations) (Fig. 4C), carbonate cement and rare pyrite nodules (Fig. 4B). Bioturbation is low to moderate (BI: 2 to 3) and increases upward in individual beds. Trace fossils consist of small Helminthopsis and Phycosiphon (<1 cm diameter) with subordinate Chondrites, Conichnus, Cosmorhaphe, Planolites and Thalassinoides (<3 cm diameter) (Fig. 9).

Interpretation.

Based on the erosional bases, normal-grading and increasing-upward bioturbation, Facies 1 is interpreted as sediment-density flow deposits. Bed type I is interpreted to represent deposition from waning, dilute, low-density turbidity currents (Lowe, 1982). The lower subdivision indicates deposition by turbulent traction transport (Stow and Piper, 1984). The middle and upper subdivisions indicate suspension settling from a waning flow. The common grain-size break between the middle and upper subdivisions suggests sediment bypass (e.g. Poyatos-Moré et al., 2016). Bed type II is interpreted to represent deposition from waxing-waning, dilute, low-density turbidity currents. The lower subdivision is interpreted as deposited from waxing flow by turbulent traction transport. The middle and upper subdivisions indicate deposition by suspension settling from waning flow. Bed type II resembles river-derived hyperpycnites (e.g. Mulder and Alexander, 2001; Mulder et al., 2003; Plink-Björlrklund and Steel, 2004; Bhattacharya and MacEachern, 2009; Zavala et al., 2011). Direct river input is also suggested by common wood fragments (Fig. 4F) and rhythmic bedding (Nakajima, 2006; Zavala et al., 2012). The low

to moderate bioturbation, small burrow size and moderate ichnodiversity suggest sea floor physicochemical stressed conditions for organisms potentially linked to a high sediment accumulation rate with frequent flow events in a fully oxygenated bottom-water environment (MacEachern et al., 2007; Bhattacharya and MacEachern, 2009; Flaig et al., 2016; Jackson et al., 2016). Moreover, common freshwater river input to the sea floor may have generated salinity fluctuations, and potentially the development of intermittent bottom-water brackish conditions. Common soft-sediment deformation suggests high sediment accumulation rate with a soft sea floor medium that is easily remobilized (Bhattacharya and MacEachern, 2009; Flaig et al., 2016).

Facies 2: mottled very thin-bedded mudstone

Description.

Facies 2 (F2) consists of light to dark grey, continuous to discontinuous, siliceous-argillaceous, fine-grained to coarse-grained bedded mudstone intercalated with dark grey, intensely bioturbated, coarse mudstone (Fig. 3D to F). Beds are 0.1 to 2 cm thick and characterized by a sharp and erosional or gradational base. Preserved sedimentary structures are identical to F1 (Fig. 3E). Bioturbation is high to intense (BI: 4 to 5) and the trace fossil assemblage is similar to F1. Burrows are usually larger (<5 cm).

Interpretation.

F2 is interpreted to be deposited by waning and waxing-waning, dilute, low-density turbidity currents, potentially derived from hyperpycnal input, based on similar sedimentological characteristics to F1. The higher bioturbation intensity and larger burrow size suggest a lower sediment accumulation rate and lower frequency of flow events in a fully oxygenated bottom-water environment. This bioturbation pattern may also be linked to a decrease in freshwater river input to the sea floor that may have led to more favourable bottom-water environment for benthic organisms (e.g. Flaig et al., 2016; Jackson et al., 2016).

Facies 3: intraclast-bearing thin-bedded to medium-bedded mudstone

Description.

Facies 3 (F3) consists of mid-grey to dark grey, siliceous-argillaceous, fine-grained to coarse-grained bedded mudstone (Figs 3G and 6A). Beds are 5 to 15 cm thick, structureless and ungraded, and characterized by a sharp and erosional base. F3 sometimes overlies partially cemented mudstone (F7) deposits (Figs 3G and 6A). Coarse mud-sized to pebble-sized mudstone clasts are common (Figs 3G and I and 6A). The pebble-sized clasts are usually concentrated in the lower part of the beds (Figs 3G and 6A). Microscopic inspection, however, shows that coarse mud-sized to sand-sized clasts are pervasive across the entire beds (Figs 3I, 6C and D). Clasts mineralogy is similar to the mudstone matrix (quartz, clay and wood fragments), but they usually contrast in colour with the surrounding matrix (Figs 3I, 6C and D). They are usually flattened with a sharp edge and a few clasts are characterized by a stringer-type texture (Fig. 3H). Some clasts are characterized by a calcium phosphate and calcium carbonate cement. The mudstone matrix does not show significant differential compaction around the mudstone clasts (Fig. 6D). Beds with mudstone clasts aligned along coarser grained horizons are observed (Fig. 6B). Pyrite aggregates are observed in the lower part of some beds (Fig. 3H). Bioturbation is low to moderate (BI: 1 to 3) and increases upward in individual beds (Fig. 6A). Trace fossils are predominantly small (<1 cm diameter) and mainly consist of Helminthopsis and Phycosiphon.

Interpretation.

The sharp and erosional base, presence of outsize mudstone clasts, and the absence of obvious grading suggest laminar flow and rapid en masse deposition by moderate-strength, cohesive debris flows (equivalent to D_{M-2} of Talling et al., 2012), preventing the development of bedforms or grading. The clasts are interpreted as rip-up mudstone intraclasts based on similar mineralogy as the mudstone matrix (e.g. Schieber et al., 2010; Schieber and Bennett, 2013). However, the colour difference between the clasts and the matrix indicates a different composition that may be linked to the presence of early cement (calcium phosphate and calcium carbonate). The texture of the pebble-sized clasts in the beds in Fig. 3H and Fig. 6A is similar to the underlying partially cemented mudstone (F7) texture. This suggests that some of these clasts may have been eroded from a sea floor characterized by early cementation processes and consolidation.

Facies 4: intraclast-bearing very thin to thin-bedded mudstone

Description.

Facies 4 (F4) consists of light grey to dark grey, siliceous-argillaceous, fine-grained to coarse-grained mudstone (Figs 3J, 7A and B). Beds are generally hard to recognize due to the absence of clear bed contacts (Fig. 7A and B). When recognized, beds are 1 to 5 cm thick with a diffuse or sharp and erosional base (Figs 3K, 7A and B). Some beds are characterized by a two-part stratigraphy: (i) thin, normally graded, coarse mudstone lower subdivision (usually less than 1 cm thick); and (ii) thicker, ungraded and structureless, coarse mudstone upper subdivision (usually 1 to 5 cm thick) with common mudstone intraclasts (Fig. 7A). Some beds are ungraded with common mudstone intraclasts. Rarely preserved continuous to discontinuous planar-parallel to low-angle laminations occur in some beds (Fig. 7B). Millimetre-thick, brown banding is observed in places (Fig. 7B). Similar to those described in F3, the mudstone intraclasts are flattened with a sharp edge and contrast in colour with the surrounding mudstone matrix (Figs 3L and 7C to E). They are, however, usually smaller (from coarse mud to fine sand-sized). Some clasts are partially cemented by calcium phosphate and calcium carbonate (Fig. 7E). No significant differential compaction is observed in the mudstone matrix around the mudstone intraclasts (Fig. 7C to E). Calcium phosphate fragments with an internal organization (parallel lines) are observed (Fig. 7F). Common rounded, coarse mud to very fine-sand-sized quartz and feldspar are also observed with differential compaction of the surrounding mudstone matrix (Fig. 7D). Pyrite nodules and carbonate-rich concretions are common. Bioturbation is low to intense (BI: 2 to 5) and the trace fossil assemblage consists of small to large (<5 cm diameter) Helminthopsis and Phycosiphon with subordinate Chondrites, Conichnus, Cosmorhaphe, Planolites and Thalassinoides.

Interpretation.

The diffuse but commonly sharp and erosional bed contacts, planar-parallel to low-angle laminations, and common mudstone intraclasts indicate deposition by sediment density flows. Beds characterized by a thin, normally graded, lower subdivision overlain by a thicker, ungraded intraclast-rich mudstone upper subdivision (Fig. 7A) may represent deposition from flows that are transitional between turbulent and laminar (Baas et al., 2009; Sumner et al., 2009; Kane and Pontén, 2012). The lower normally-graded section may represent deposition by turbulent flow while the upper ungraded and intraclast-rich

section may represent deposition by laminar flow. Ungraded beds with mudstone intraclasts may represent rapid en masse deposition by low-strength, cohesive debris flows (equivalent to D_{M-1} of Talling et al., 2012). The rare, planar-parallel to low-angle laminations suggest turbulent transport, potentially by dilute, low-density turbidity currents. Similar to F3, the mudstone intraclasts are interpreted to be eroded from partially consolidated sea floor sediments. Calcium-phosphate fragments with an internal organization are interpreted as reworked bone fragments. The low to intense bioturbation intensity, large burrow size, and high ichnodiversity indicate relatively low sediment accumulation rate and low frequency of flow events in a fully oxygenated bottom-water environment.

Facies 5: homogenous mudstone

Description.

Facies 5 (F5) consists of light grey to mid-grey, siliceous-argillaceous, fine-grained to medium-grained mudstone (Fig. 3M and N). No bed contacts are recognized. Similar to F3 and F4, coarse mud to fine sand-sized mudstone intraclasts are observed (Fig. 3O). Bioturbation has destroyed all primary sedimentary structures (BI: 6) and the trace fossil assemblage consists of small to large (<5 cm diameter) Helminthopsis and Phycosiphon with subordinate Cosmorhaphe, Planolites and Teichichnus (Fig. 9).

Interpretation.

The absence of preserved bed boundaries and physical sedimentary structures prevent an interpretation of the primary sedimentary processes. The observed mudstone intraclasts suggest either: (i) primary deposition dominantly en masse from low-strength cohesive debris flows (similar to F3 and part of F4); or by (ii) transitional flows (similar to F4). Deposition by dilute, low-density turbidity currents (similar to F1 and F2) or by vertical suspension fallout cannot be ruled out where mudstone intraclasts are not identified. Following deposition, sediment was homogenised by bioturbation, indicating deposition in a fully oxygenated bottom-water environment with low sediment accumulation rate.

Facies 6: carbonaceous mudstone

Description.

Facies 6 (F6) consists of dark grey to black, carbonaceous-argillaceous-siliceous, fine-grained to coarse-grained mudstone (Fig. 3P). Diffuse bed boundaries and remnant planar-parallel to low-angle laminations are suggested by thin-section observation (Fig. 3Q). No obvious grading is observed. Rare mudstone intraclasts and coarse mud to very fine sand-sized quartz and feldspar are recognized (Fig. 3R). The mudstone matrix shows differential compaction around the outsize quartz and feldspar (Fig. 3R). The concentration of carbonate-rich concretions and pyrite nodules is the highest of the succession (Fig. 2). This facies is characterized by an orthoconic nautiloid that represents the only macrofossil preserved in the succession. Bioturbation is moderate to intense (BI: 3 to 5) and the trace fossil assemblage is exclusively composed of very small (<1 mm diameter) Helminthopsis and Phycosiphon (cryptobioturbation).

Interpretation.

Diffuse bed boundaries and outsize grains indicate deposition influenced by sediment density flows. The common presence of carbonate-rich concretions and only rarely observed physical sedimentary structures, however, suggest dominant low energy processes. The presence of mudstone intraclasts and outsized grains suggests occasional deposition en masse by low-strength, cohesive debris flows or by transitional flows. The presence of the orthoconic nautiloid, which does not show evidence of transport, suggests deposition by vertical suspension fallout for part of this facies. Significant breaks in sediment accumulation took place to account for the development of carbonate-rich concretions (Taylor and Curtis, 1995). The pervasive presence of cryptobioturbation, the very low ichnodiversity and the very small burrow size all point toward deposition in a dysoxic bottom-water environment.

Facies 7: partially cemented mudstone

Description.

Facies 7 (F7) consists of light grey to mid-grey partially cemented mudstone (Fig. 3S to U). Cement consists of calcium carbonate and calcium phosphate. No physical sedimentary structures are recognized. Bioturbation is intense (BI: 6) and the trace fossil assemblage is dominated by large (<5 cm

diameter) Helminthopsis and Phycosiphon with subordinate Chondrites, Conichnus, Cosmorhaphe and Planolites (Fig. 9).

Interpretation.

The high cement content and intense bioturbation suggests a significant break in sediment accumulation rate that is associated with early diagenetic processes (Taylor and Curtis, 1995). These levels could potentially be associated with starved basin floor condensed horizons.

Facies 8: deformed deposits

Description.

Facies 8 (F8) consists of 5 to 6-m-thick, deformed material (Fig. 8A and B) stratabound by undeformed units. Three distinct deformed intervals are recognized in the core (Fig. 2). The lower deformed interval is 6.6 m thick (from 725.50 to 718.90 m; Fig. 2) and is dominated by plastic deformation with common soft-sediment deformation (Fig. 8A). Decimetre-thick blocks of ash-rich sandstone (F9) and macroscopic mudstone intraclasts similar to those described in F3 are observed (Fig. 3V and W). The middle deformed interval is 5 m thick (from 714.50 to 709.50 m; Fig. 2) and is characterized by a combination of plastic and brittle deformation (Fig. 8B). Plastic deformations consist of soft-sediment deformation (Fig. 3X). Brittle deformations consist of normal faults (mainly listric) and reverse faults with common fractures (Fig. 3Y). The upper deformed interval is 5.65 m thick (from 595.25 to 589.60 m; Fig. 2) and is characterized by intense brittle and plastic deformation similar to that of the middle-deformed section. Internal facies and trace fossils are similar to the rest of the stratigraphy.

Interpretation

The presence of both brittle and plastic deformation in stratabound units indicates slump or slide processes, and sea floor remobilization. The autochthonous nature of the material (facies and trace fossil assemblage) suggests an intrabasinal origin and relatively short travel distance.

Facies 9: ash-rich sandstone.

Description.

Facies 9 (F9) consists of ash-rich sandstone beds. Beds are 1 to 15 cm thick, sharp, erosional and normally graded (Fig. 3Z). The lower part of the bed usually consists of planar-parallel to low-angle current ripple laminated, very fine-grained sandstone. The middle part of the bed consists of normally graded, structureless sandstone with rare soft-sediment deformation. The upper part of the bed is strongly bioturbated and consists of fine-grained to medium-grained mudstone. Post-depositional cementation is common. Some observed carbonate-rich concretions (Fig. 2) may correspond to completely cemented, ash-rich sandstone beds.

Interpretation.

Based on the erosional base, normal grading and planar-parallel to low-angle laminations, the ash-rich sandstone beds are interpreted to be deposited by ash-rich, low-density turbidity currents. The higher porosity and permeability of this facies compared to the muddy facies may explain its preferential cementation.

Depositional environments

The range of depositional processes described here—low-density turbidity currents, debris flows, transitional flows, slumps and slides, and vertical suspension fallout, in combination with the stratigraphic context of overlying basin floor fans—suggests that this succession was deposited in a lower slope to basin-floor environment strongly influenced by sediment-density flows. The common slumps, slides, and tilted intervals (Fig. 2) suggest localized tilting and post-depositional sediment remobilization. The absence of wave-generated structures indicates deposition below storm wave-base. A deep-water environment is also suggested by the trace fossil assemblage (dominance of Helminthopsis and Phycosiphon with subordinate Chondrites, Conichnus, Cosmorhaphe, Planolites, Teichichnus and Thalassinoides; Fig. 9) that has been described in other deep-water marine successions (e.g. Loucks and Ruppel, 2007; Hubbard et al., 2009; Knaust and Bromley, 2012; Heard et al., 2014). The overall trace fossil assemblage is consistent with the distal Cruziana to proximal Zoophycus ichnofacies (MacEachern et al., 2007). The ichnodiversity is relatively low but bioturbation

intensity is highly variable (BI: 2–6; Fig. 2), suggesting intermittently stressed sea floor physicochemical conditions (MacEachern et al., 2007; Bhattacharya and MacEachern, 2009). Following deposition, the soft sediment was colonized by deposit-feeding and surface-grazing organisms (Bhattacharya and MacEachern, 2009).

Primary mud is interpreted to have been sourced via deltaic input based on the dominance of detrital grains (quartz, feldspar, mica), and common wood fragments. The location and size of the sediment delivery system is unknown due to uplift and erosional removal of the time equivalent shelf during the Cape Fold Belt orogeny during the Triassic. The absence of sand delivery into the system except for the ash-rich sandstone (F9) may be explained by: i) a dominance of mud-grade sediment delivered to the basin; or ii) a distal position relative to the feeder systems and/or time-equivalent sandstone deposits.

Depositional units

The 538.50-m-thick studied succession shows a repeatable, consistent arrangement of facies into 2–26-m-thick depositional units (Figs 2 and 10).

Description

The base of a depositional unit is defined at the transition (abrupt to gradational) from intraclast-bearing, very thin- to thin-bedded mottled mudstone (F4), homogenous mudstone (F5) or carbonaceous mudstone (F6) to very thin-bedded mudstone (F1) or more rarely mottled very thin-bedded mudstone (F2), that is marked by a dark to light colour change (Fig. 10). This transition is also marked by an abrupt decrease in bioturbation intensity and TOC (Fig. 10). The lower part of a unit is dominated by F1 intercalated with rare F2, muddy deformed deposits (F8) and tilted intervals. Beds usually thin upward and gradually become more bioturbated (transition from F1 to F2). Some rare units are characterized by a lower part dominated by mottled, very thin-bedded mudstone (F2) grading into very thin-bedded mudstone (F1) and then grading back into F2 (from 816.50 m up to 806 m for example; Fig. 2). In the unit targeted for TOC analysis, the lower part TOC values increase upward and range from 0.62 to 1.72 wt.% with an average of 0.93 wt.% TOC (n = 23) (Fig. 10).

In the upper part of the units, F2 grades to darker intraclast-bearing, very thin- to thin-bedded mottled mudstone (F4) and carbonaceous mudstone (F6) intercalated with rare mottled very thin-bedded

mudstone (F2), homogenous mudstone (F5), intraclast-bearing, thin- to medium-bedded mudstone (F3), and partially cemented mudstone (F7). The intensity of bioturbation, burrow size, concentration of pyrite and carbonate-rich concretions are usually higher than in the lower part of the units (Figs 2 and 10). However, grain-size is similar between the lower and upper parts. The upper part TOC values are higher and range from 1.06 to 2.28 wt.% with an average of 1.71 wt.% (n = 19) (Fig. 10). Ash-rich sandstone beds (F9) are found in both the lower and upper parts of the units (Figs 2 and 10).

Interpretation

These repeated and relatively well-organized mudstone depositional units show some variability in thickness and facies-stacking pattern (Fig. 2), but all contain a lower part dominated by facies interpreted to record dilute, low-density turbidity currents, potentially derived from hyperpycnal input (F1, F2), together with occasional sediment remobilization (F8). The upper part is dominated by more bioturbated and organic-rich facies with common mudstone intraclasts (F3 to F6), interpreted as transitional flows and debris flow deposits with scarce indicators of suspension fallout processes.

The low bioturbation intensity and small burrow size in the lower part of a depositional unit (dominated by F1 and F2) suggest bottom-water physicochemically stressed conditions that may be linked to high sediment accumulation rate from relatively frequent low-density turbidity currents (Fig. 11) (e.g. MacEachern et al., 2007; van der Kolk et al., 2015). Freshwater input from hyperpycnal flows may have decreased bottom-water salinity and increased the stressed conditions for benthic organisms (e.g. MacEachern et al., 2007; Flaig et al., 2016). The deformed deposits (F8) suggest occasional and localized shelf or slope instabilities (Fig. 11) which may be related to the interpreted high sediment flux. The high sediment accumulation rate is also suggested by common soft-sediment deformations (Fig. 4C) and tilted intervals (Fig. 10). The vertical transition from F1 to F2 associated with an increase in bioturbation intensity and burrow size and a decrease of bed thickness (Fig. 12) suggests a gradual decrease in hyperpycnal flow activity with more time available between depositional events for benthic organisms to disturb the primary sedimentary fabric (e.g. Wetzel, 1991; MacEachern et al., 2007; Heard et al., 2014). The decrease in direct freshwater river input may have led to an increase of bottom-water salinity, therefore, decreasing bottom-water stressed conditions. The rare units characterized by F2 grading into F1 and grading into F2 suggests waxing-then-waning sediment flux.

The higher bioturbation intensity, bigger burrow size and organic enrichment of the debrites and

transitional flow deposits (F3 to F6) in the upper part of the depositional units suggest lower sediment accumulation rate and frequency of flow events (Fig. 12). The debris flows and transitional flows may have originated from shelf or slope instabilities (Fig. 11) or from the transformation of low-density turbidity currents (e.g. Kane et al., 2017). The more common carbonate-rich concretions and partially cemented mudstone (F7) indicate occasional depositional breaks associated with early diagenetic processes and condensed horizons.

These observations suggest a gradual decrease in sediment accumulation rate and frequency of flow events at the scale of a single depositional unit (Fig. 12) associated with a decrease in physicochemical-stressed bottom-water conditions. The lower part of a depositional unit dominated by low-density turbidites therefore represents relatively proximal deposits related to high rates of sediment input while the upper part, dominated by transitional flow deposits and debrites, represents deposition in a more distal or lateral position (Fig. 11). No significant grain size variations are observed between the lower and upper part of a depositional unit, which suggests no major variations of sediment calibre supplied to the deep-water environment. Possible controls on facies stacking pattern and unit organisation are discussed below.

DISCUSSION

The record of hyperpycnal flows in deep-water mudstones

Hyperpycnal flow processes are interpreted to be common in the lower part of the depositional units (Figs 10 and 12) marked by inversely-to-normally graded sections in bed type II on F1 (Fig. 4E). The co-occurrence of both normally graded beds (bed type I) and inversely-to-normally graded beds (bed type II) in F1 may be explained by the evolution of the flow structure during a sediment-density-flow event. In distal basinal locations, the faster moving part of a hyperpycnal flow (generated during the river flood peak discharge) tends to overtake the slower moving part of the flow such that the velocity distribution pattern is similar to that of a surge-type current (Kneller and McCaffrey, 2003). As a consequence, waxing-waning flow is usually only preserved in proximal location whereas distal basinal location only records waning flow, and the resulting deposits resemble classic low-density turbidites (Kneller and McCaffrey, 2003). Both normally graded and inversely-to-normally graded beds, however,

have been observed 700 km away from a river mouth in the Central Japan Sea (Nakajima, 2006). The latter study proposed that the presence of inversely-to-normally graded beds in such a distal basinal location was explained by a long-term lag between the beginning and the peak discharge of the flow such that the faster moving part of the flow does not overtake the slower moving part of the flow within the travel distance between the river mouth and the site of deposition.

It is proposed that the relatively scarce (but usually thicker) inversely-to-normally graded bed type II may have been deposited during larger flood events while the more common normally graded bed type I may have been deposited by lower-magnitude floods. A waxing-waning flow depositing bed type II is expected to wane in distal positions depositing normally graded beds (similar to bed type I). Bed type I and II may, therefore, be genetically linked and bed type I may represent the distal expression of bed type II (Fig. 13A). The common sharp contact between the middle and upper subdivisions in bed type I (Figs 4D and 5) may indicate that sediment was bypassed to more distal locations. Bed type I without a bypass surface may, therefore, represent the distal-most expression of river-derived turbidity currents recognized in this succession (Fig. 13A). Another potential mechanism for the deposition of bed type I is related to surge-type intrabasinal flows, induced by gravitational failure following rapid deposition of sediments in the delta front or slope during a flood event (Talling et al., 2013). This process, however, cannot account for the development of waxing-waning flows and the deposition of inversely-to-normally graded bed type II.

Hyperpycnites are widely described in the marine realm from shelf to basin-floor environments (Nemec, 1995; Mutti et al., 2003; Plink-Björlrklund and Steel, 2004; Petter and Steel, 2006; Bhattacharya and MacEachern, 2009; Zavala et al., 2011; Van der Kolk et al., 2015). This type of deposit may be more common than previously thought in the mudstone record as noted previously by Soyinka and Slatt (2008). A careful microscopic characterisation of thin beds—grading, sedimentary structures, stacking pattern, continental organic fragment content—may, therefore, help to recognize evidence for deposition by hyperpycnal flows in deep-water mudstones.

Origin and transport of mudstone intraclasts

A common feature recognized in F3, F4, F5 and F6 in the upper part of a depositional unit (Figs 10 and

12) is the presence of mudstone intraclasts. Recent studies have demonstrated that mudstone intraclasts are relatively common in mudstone successions deposited in a wide range of environments and that they can be eroded from water-rich mudstone at the sea floor, transported for tens to hundreds of kilometres as bed load, and deposited when the flow decelerates (Schieber et al., 2010; Plint et al., 2012; Schieber and Bennett, 2013; Plint, 2014; Schieber, 2016). When mudstone intraclasts are abundant, a diagnostic microscopic lenticular fabric is observed within the resultant deposits (e.g. Schieber et al., 2010; Schieber, 2016). Mudstone intraclasts can also form lags at the base of beds (e.g. Schieber, 1998; Plint et al., 2012). However, the deep-water mudstone facies described here are devoid of a lenticular fabric and the mudstone intraclasts are usually scattered in centimetre to decimetre thick beds rather than concentrated as lags. The interpreted range of depositional processes transporting and depositing these intraclasts (debris flows and transitional flows) have been observed in coarser grained, deep-water sediments from the Gulf of Mexico (Kane and Pontén, 2012). Kane et al. (2017) have shown that a turbulent flow can evolve into a debris flow (laminar) or a transitional flow with the entrainment of sea floor mud and flow deceleration. Here, the mudstone intraclasts are found mainly in the upper part of the depositional units interpreted to be deposited in a distal or lateral position relative to sediment input (Fig. 11). They are flattened but do not show bending or squeezing between more resistant particles. Moreover, some mudstone intraclasts are partially cemented by calcium phosphate and calcium carbonate. Post-depositional bioturbation of the clasts is usually limited compared to the mudstone matrix. Mechanisms for the incorporation, transport and deposition of these mudstone intraclasts (Fig. 13B) are:

1 Because of the interpreted distal or lateral position relative to the sedimentation input (Fig. 11), time was available between sediment density flows for early consolidation of mud on the sea floor (either on the shelf, the slope, or the basin-floor). This process is interpreted to generate the consolidation of the partially cemented mudstone (F7). Early consolidation of pre-compacted sea floor mud may have occurred due to bacterial mediated precipitation of calcite and phosphate cements in the pore space (Curtis, 1980; Plint and Macquaker, 2013).

2 Occasional muddy-sediment-density flows (turbulent or laminar) may have been triggered through shelf or slope instabilities (Fig. 11).

554 **3** These sediment density flows may have eroded and entrained mudstone clasts from the partially
555 consolidated sea floor (Figs 3G and 6A). These rip-up intraclasts may have travelled for tens to
556 hundreds of kilometres (e.g. Schieber, 2010) and may have been abraded and disintegrated due to
557 particle collision.
558
559 **4** The generation of smaller particles may have increased cohesion of the flow, triggering
560 transformation into a debris flow (laminar) or transitional flow (laminar and turbulent) (Baas et al.,
561 2009; Sumner et al., 2009; Kane et al., 2017). Flow transformation may have also occurred due to
562 flow deceleration linked to the presence of sea floor topography (Sumner et al., 2009).
563
564 5 Depending on the flow state during flow deceleration, either debrites or transitional flow deposits
565 were preserved.
566
567 **6** The relatively flat shape of the mudstone intraclasts suggests that they were subsequently
568 compacted during burial (Schieber, 2016). Alternatively, the clasts may have been eroded from
569 consolidated sea floor mudstone as relatively flat rip-up intraclasts. The limited post-depositional
570 bioturbation of the mudstone intraclasts compared to the mudstone matrix suggests that they were
571 deposited as partially consolidated particles, to be able to resist biogenic disruption.
572
573 Debrites and transitional flow deposits have also been recently recognized in other deep-water
574 mudstone successions (Konitzer et al., 2014; Harazim and McIlroy, 2015; Newport et al., 2018).
575 Therefore, these energetic flows, usually associated with sandy deep-water systems, may be more
576 common in deep-water mudstone successions than previously thought. Moreover, distal or lateral
577 positions, usually interpreted to be characterized by vertical suspension fallout processes in deep-water
578 environments, may include significant volumes of the deposits of higher energy sediment density flow
579 processes.
580
581

Allogenic and autogenic controls on the depositional units

The vertical facies stacking pattern observed within a single depositional unit may be related to allogenic and/or autogenic controls, both of which are discussed below. The upward increase in bioturbation intensity, burrow size and early cementation processes within most depositional units is interpreted to represent a decrease in sediment accumulation rate and frequency of flow events (Fig. 12). This suggests deposition in a gradually more distal or lateral environment relative to the sediment input.

A commonly presented allogenic control on deep-water systems is relative sea-level (e.g. Posamentier et al., 1991; Posamentier and Kolla, 2003; Flint et al., 2011). The usually sharp base to each depositional unit, with dominance of hyperpycnal flows and low bioturbation (Figs 10 and 12) can be interpreted as consistent with times of lowered sea-level. Hyperpycnal flows preferentially develop during lowstand when deltas are at the shelf edge or at the canyon head, providing a frequent supply of low-density turbidity currents downslope (e.g. Mitchum et al., 1977; Mutti, 1985; Shanmugam et al., 1985; Mutti and Normak, 1991; Posamentier et al., 1991). Moreover, muddy sediments near the shelf edge at lowstand are prone to collapse, generating mass-wasting processes, possibly recorded by the deformed deposits (F8). The collapse scars generated on the shelf edge or the slope may have acted as conduits for hyperpycnal flow, thus increasing runout distance (Henriksen et al., 2011). Other authors have proposed that hyperpycnal flow activity decreases at lowstand because rivers tend to merge and drain larger catchment areas, which decreases the river sediment load (Mulder and Syvitski, 1995, 1996). The usually low bioturbation intensity, small burrow size and common instability indicators (soft sediment deformations, tilting) in the interpreted hyperpycnites (F1 and F2; Figs 10 and 12) suggest a high frequency of flow events and a high sediment accumulation rate that are more likely to occur during relative sea-level fall.

The upper part of a depositional unit is always dominated by more bioturbated debrites and transitional flow deposits (Figs 2, 10 and 12). The interpreted lowered sediment flux to the deep-water environment is consistent with the reduced sediment supply expected during highstands of relative sea level, due to increased shelf accommodation and sediment storage. This reduction in sediment supply may have promoted early consolidation of sea floor mud, and occasional sediment density flows derived from shelf or slope instabilities may have reworked the sea floor to deposit rip-up mudstone intraclasts. Highstands in deep-water environments are usually characterized by anoxic to dysoxic conditions, high

611 TOC content and common pyrite (e.g. Wignall, 1994; Bohacs, 1998; Abouelresh and Slatt, 2012; Ayranci
612 et al., 2018b). Hemipelagic and pelagic vertical suspension fallout is usually the dominant interpreted
613 depositional processes with only rare sediment-density flows (e.g. Konitzer et al., 2014). The dataset for
614 this study strongly challenges this generalized model insofar as the upper part of each depositional unit
615 is mostly characterized by the product of sediment-laden flows (mostly debris flows and transitional
616 flows; Fig. 12). Moreover, the pervasive presence of bioturbation indicates a persistent oxygenated sea
617 floor. Recent studies of shelf mudstone successions indicate the presence of active sedimentary
618 processes (storms, geostrophic currents, wave-enhanced gravity flows) that re-suspend previously
619 deposited mud to generate turbidity currents moving downslope by gravity (Ichaso and Dalrymple, 2009;
620 Macquaker et al., 2010; Denommee et al., 2016; Poyatos-Moré et al., 2016; Birgenheier et al., 2017).
621 Shelf sedimentary processes may therefore have generated intermittent sediment density flows, which
622 reached basin-floor environments in the Lower Ecca Group during highstand conditions, allowing
623 oxygenation of the sea floor.

624 Another common mechanism controlling deep-water stacking pattern is autogenic
625 compensational stacking (e.g. Mutti and Sonnino, 1981; Deptuck et al., 2008; Prélat et al., 2009; Prélat
626 and Hodgson, 2013). In this model, successive muddy low-density turbidites (F1 and F2) created
627 depositional topography. Through time, the generation of topography may have re-routed later low-
628 density turbidity currents laterally into topographic lows. Due to the gradual decreasing sediment flux, in
629 a vertical 1D stratigraphic section, bed thickness is expected to decrease upward, while bioturbation
630 intensity and burrow size are expected to increase, as observed in our dataset within a single
631 depositional unit (Figs 10 and 12). The high bioturbation intensity and larger burrows observed in the
632 upper part of the depositional units (dominated by F3 to F7) may, therefore, be related to a more lateral
633 position relative to the sediment entry point (Fig. 11). In this environment further from the main sediment
634 input, the lower sediment accumulation rate may have favoured early consolidation of sea floor mud and
635 the growth of early cements with occasional erosion and entrainment of rip-up intraclasts by flows
636 derived from shelf or slope instabilities. The usually abrupt base of the overlying unit (Fig. 10) may
637 indicate avulsion of the sediment entry point in the upstream part of the system (e.g. Gervais et al.,
638 2006; Prélat et al., 2009).

639 In summary, the well-ordered and repeated nature of the depositional units is consistent with a

regular control mechanism. The 1D nature of the core dataset limits the analysis of autogenic and allogenic controls, which requires regional mapping of units and key surfaces to assess whether the strongly organized nature of the stratigraphy is present at a larger scale.

Stacking pattern of depositional units

The thickness of depositional units and proportion of facies vary stratigraphically (Fig. 2). This stacking pattern is interpreted to record long-term changes in depositional conditions in the deep-water environment of the Karoo Basin. The core succession is linked to existing lithostratigraphy (Johnson et al., 2006), based on sedimentological and stacking pattern differences (Fig. 2). The dominance of carbonaceous mudstone (F6) in the Prince Albert and Whitehill formations (Fig. 2) suggests a distal position relative to the sediment entry point. This is also suggested by common concretions (Fig. 2). The upward decreasing proportion of F6, increasing proportion of very thin-bedded mudstone (F1) and mottled very thin-bedded mudstone (F2), and increasing depositional units thickness in the Collingham and lower Tierberg formations suggest a progressive increase of energy in the deep-water environment, likely produced by long-term progradation of the sediment delivery system. The middle Tierberg Formation records the thickest depositional units and the lowest bioturbation intensity of the succession. The proportion of F1 and F2 within each depositional unit is the highest of the succession. Indicators of sediment instability (deformed deposits and tilted intervals) are also common. This part of the succession, therefore, records the highest energy conditions and sediment flux associated with the maximum progradation. Decreasing unit thickness in the upper Tierberg Formation, associated with the decreasing proportion of F1 and F2, increasing bioturbation intensity and transition from coarse to fine mudstone, suggests decreasing sediment flux consistent with a retrogradation of the sediment delivery system. The decreasing grain size could also be related to a change of sediment calibre delivered to the deep-water environment, linked to a major rearrangement of the basin margin.

To summarize, the stacking pattern of successive depositional units indicate a long-term progradation of the sediment delivery system, followed by a major retrogradation, before the emplacement of the overlying sandy basin floor fans of the Skoorsteenberg Formation (Johnson et al., 2001; Hodgson et al., 2006). This demonstrates that a detailed multi-scale characterization of thick and

continuous deep-water mudstone successions may help to evaluate the evolution of depositional conditions within deep-water environments.

CONCLUSIONS

This study documents an exceptionally thick and continuous deep-water mudstone succession from the Permian Karoo Basin. The combination of macroscopic and microscopic descriptions allowed for the definition of nine sedimentary facies deposited by a wide range of processes—low-density turbidity currents, debris flows, transitional flows, slumps, slides, vertical suspension fallout—in a dominantly oxic to dysoxic environment. Facies stack to produce repeated and well-organized 2 to 26-m-thick depositional units. Each unit is characterized by a lower part dominated by low-density turbidites, with evidence for hyperpycnal flow processes and sediment remobilization, and an upper part dominated by debrites and transitional flow deposits with common mudstone intraclasts. These units show an internal upward increase in bioturbation intensity, burrow size, total organic carbon, and early cementation processes interpreted to indicate a gradual decrease in sediment accumulation rate and frequency of flow events. This vertical pattern suggests deposition in gradually more distal or lateral environments relative to the sediment input. At the larger scale, successive depositional units thicken-upward and then thin- upward, interpreted to represent a long-term progradational to retrogradational stratigraphic trend. This thick deep-water mudstone successions contains no clear evidence for volumetrically significant deposition by pelagic and hemipelagic suspension fallout, challenging the traditional view that deep-water mud are deposited by slow rainout in quiescent environments. Conversely, this study suggests that most deep-water mud can be transported and deposited by tractive transport processes along continental margins, which has implications for the correct interpretation of time of clastic starvation and depositional rates in deep-water environments. More systematic descriptions of deep-water mudstones using a range of techniques—conventional core logging, optical microscopy, electron microscopy, ichnology—similar to the characterization of shallow-water mudstones is, therefore, needed to fully capture their heterogeneity, which may also have a major impact on seal capacity or unconventional reservoir characterization, as well as on palaeoenvironmental reconstructions.

ACKNOWLEDGMENTS

The work presented here is part of the SLOPE Project, Phase 4. We thank the consortium of sponsors (Anadarko, BHPBilliton, BP, CNOOC-Nexen, ConocoPhillips, Equinor, Maersk, Murphy, Neptune Energy, Petrobras, Premier Oil, Shell, Total, VNG Norge and Woodside) for financial support. We also thank the AAPG Foundation Grant-in-Aid program for the award of the Institut Francais du Pétrole Grant, which part-funded this project. We thank De Ville Wickens for field support and the Karoo farmers for access to their land. We thank Andy Connelly for support for the geochemical analysis and for the access to the Cohen Laboratory at the University of Leeds. Rachel Healy, Charlotte Allen and Luz Gomis Cartesio are thanked for their assistance in the core store. The manuscript greatly benefited from thorough and constructive reviews by Associate Editor Kyle Straub and two anonymous reviewers.

References

Abouelresh, M.O. and **Slatt, R.M.** (2012) Lithofacies and sequence stratigraphy of the Barnett Shale in east-central Fort Worth Basin, Texas. AAPG Bull., **96**, 1–22.

Andersson, P.O.D. and **Worden, R.H.** (2004) Mudstones of the Tanqua Basin, South Africa: an analysis of lateral and stratigraphic variations within mudstones, and a comparison of mudstones within and between turbidite fans. Sedimentology, **51**, 479–502.

Ayranci, K., Harris, N.B. and **Dong, T.** (2018a) Sedimentological and ichnological characterization of the Middle to Upper Devonian Horn River Group, British Columbia, Canada: Insights into mudstone depositional conditions and processes below storm wave base. J. Sed. Res., **88,** 1-23.

Ayranci, K., Harris, N.B. and **Dong, T.** (2018b) High resolution sequence stratigraphic reconstruction of mud-dominated systems below storm wave base; a case study from the Middle to Upper Devonian Horn River Group , British Columbia , Canada. Sed. Geol., **373**, 239–253.

Baas, J.H., **Best, J.L**., **Peakall, J**. and **Wang, M**. (2009) A phase diagram for turbulent, transitional, and laminar clay suspension flows. J. Sed. Res., **79**, 162–183.

Bangert, B., Stollhofen, H., Lorenz, V. and **Armstrong, R.A**. (1999) The geochronology and

722 significance of ash-fall tuffs in the glaciogenic Carboniferous-Permian Dwyka Group of Namibia and
723 South Africa. J. Afr. Earth Sci., **29**, 33–49.

724 **Belica, M.E., Tohver, E., Poyatos-Moré, M., Flint, S.S., Parra-Avila, L., Lanci, L., Denyszyn, S**. and
725 **Pisarevsky, S**. (2017) Refining the chronostratigraphy of the Karoo Basin, South Africa:
726 magnetostratigraphic constraints support an Early Permian age for the Ecca Group. Geopys. J. Int., **211**,
727 1354–1374.

728 **Bhattacharya, J.P.** and **MacEachern, J.A**. (2009) Hyperpycnal rivers and prodeltaic shelves in the
729 Cretaceous Seaway of North America. J. Sed. Res., **79**, 184–209.

730 **Birgenheier, L.P., Horton, B., McCauley, A.D., Johnson, C.L**. and **Kennedy, A**. (2017) A depositional
731 model for offshore deposits of the lower Blue Gate Member, Mancos Shale, Uinta Basin, Utah, USA.
732 Sedimentology, **64**, 1402–1438

733 **Blewett, S.** and **Phillips, D**. (2016) An overview of cape fold belt geochronology: implications for
734 sediment provenance and the timing of orogenesis. In: Origin and Evolution of the Cape Mountains and
735 Karoo Basin (Eds B. Linol and M. Wit), pp. 45–55. Springer, Cham,.

736 **Bohacs, K.M.** (1998) Contrasting expressions of depositional sequences in mudrocks from marine to
737 non marine environments. In: Shales and Mudstones (Eds J. Schieber, W. Zimmerle and P.S. Sethi),
738 pp. 33–78. E. Schweizerbart'sche, Stuttgart,.

739 **Bohacs, K.M., Lazar, R.O**. and **Demko, T.M**. (2014) Parasequence types in shelfal mudstone strata-
740 Quantitative observations of lithofacies and stacking patterns, and conceptual link to modern
741 depositional regimes. Geology, **42**, 131–134.

742 **Bromley, R.G.** (1996) Trace Fossils: Biology, Taphonomy and Applications, Second Edition. Chapman
743 and Hall, London, 361 pp.

744 **Buatois, L.A., Netto, R.G.** and **Mángano, M.G**. (2010) Ichnology of late Paleozoic postglacial
745 transgressive deposits in Gondwana: reconstructing salinity conditions in coastal ecosystems affected
746 by strong meltwater discharge. In: Late Paleozoic Glacial Events and Postglacial Transgressions in
747 Gondwana (Eds O. Lopez Gamundi and L.A. Buatois), Geol. Soc. Am. Spec. Pap., **468**, 149–173.

748 **Catuneanu, O., Hancox, P.J.** and **Rubidge, B.S.** (1998) Reciprocal flexural behaviour and contrasting

749 stratigraphies: a new basin development model for the Karoo retroarc foreland system, South Africa.
750 Basin Res., **10**, 417–439.

751 **Chukwuma, K.** and **Bordy, E.M.** (2016) Spatiotemporal sedimentary facies variations in the Lower
752 Permian Whitehill Formation, Ecca Group, Karoo Basin In: Origin and Evolution of the Cape Mountains
753 and Karoo Basin (Eds B. Linol and M. Wit), pp. 101-110. Springer, Cham,

754 **Curtis, C.D.** (1980) Diagenetic alteration in black shales. J. Geol. Soc., **137**, 189-194.

755 **De Wit, M.J.** and **Ransome, I.G.D.** (1992) Regional inversion tectonics along the southern margin of
756 Gondwana. In: Inversion tectonics of the Cape Fold Belt, Karoo and Cretaceous basins of Southern
757 Africa (Eds M.J De Wit and I.G.D Ransome), pp. 15-21. A.A. Balkema, Rotterdam.

758 **Denommee, K.C., Bentley, S.J., Harazim, D.** and **Macquaker, J.H.S.** (2016) Hydrodynamic controls
759 on muddy sedimentary-fabric development on the Southwest Louisiana subaqueous delta. Mar. Geol.,
760 **382**, 162–175.

761 **Deptuck, M.E., Piper, D.J., Savoye, B.** and **Gervais, A.** (2008) Dimensions and architecture of late
762 Pleistocene submarine lobes off the northern margin of East Corsica. Sedimentology, **55**, 869-898.

763 **Dixon, J.F., Steel, R.J.** and **Olariu, C.** (2012) River-dominated, shelf-edge deltas: delivery of sand
764 across the shelf break in the absence of slope incision. Sedimentology, **59**, 1133–1157.

765 **Egenhoff, S.** and **Fishman, N.** (2013) Traces in the dark - sedimentary processes and facies gradients
766 in the Upper Devonian - Lower Mississippian Upper Shale Member of the Bakken Formation, Williston
767 Basin, North Dakota, USA. J. Sed. Res., **83**, 803–824.

768 **Faure, K.** and **Cole, D.I.** (1999) Geochemical evidence for lacustrine microbial blooms in the vast
769 Permian Main Karoo, Parana, Falkland Islands and Huab basins of southwestern Gondwana.
770 Palaeogeogr. Palaeoclimatol. Palaeoecol., **152**, 189–213.

771 **Flaig, P.P., Hasiotis, S.T.** and **Jackson, A.M.** (2016) An Early Permian, paleopolar, postglacial, river-
772 dominated deltaic succession in the Mackellar-Fairchild formations at Turnabout Ridge, Central
773 Transantarctic Mountains, Antarctica. Palaeogeogr. Palaeoclimatol. Palaeoecol., **441**, 241-265.

774 **Geel, C., Schulz, H.M., Booth, P., De Wit, M**. and **Horsfield, B**. (2013) Shale gas characteristics of
775 Permian black shales in South Africa: results from recent drilling in the Ecca Group (Eastern Cape).

776 Energy Procedia, **40**, 256–265.

777 **Gervais, A., Savoye, B., Mulder T.** and **Gonthier, E.** (2006) Sandy modern turbidite lobes: a new
778 insight from high resolution seismic data, Mar. Petrol. Geol., **23(4)**, 485-502.

779 **Gomis-Cartesio, L.E., Poyatos-Moré, M., Flint, S.S., Hodgson, D.M., Brunt, R.L.** and **Wickens,**
780 **H.d.V.** (2016) Anatomy of a mixed-influence shelf edge delta, Karoo Basin, South Africa. Geol. Soc.
781 London Spec. Publ., **444**, 393–418.

782 **Gomis-Cartesio, L.E., Poyatos-Moré, M., Hodgson, D.M.** and **Flint, S.S.** (2018) Shelf-margin
783 clinothem progradation, degradation and readjustment: Tanqua depocentre, Karoo Basin (South Africa).
784 Sedimentology, **65**, 809–841.

785 **Götz, A.E., Ruckwied, K.** and **Wheeler, A.** (2018) Marine flooding surfaces recorded in Permian black
786 shales and coal deposits of the Main Karoo Basin (South Africa): implications for basin dynamics and
787 cross-basin correlation. Int. J. Coal Geol., **190**, 178-190.

788 **Harazim, D.** and **McIlroy, D.** (2015) Mud-rich density-driven flows along an Early Ordovician storm-
789 dominated shoreline: implications for shallow-marine facies models. J. Sed. Res., **85**, 509–528.

790 **Heard, T.G., Pickering, K.T.** and **Clark, J.D**. (2014) Ichnofabric characterization of a deep-marine
791 clastic system: a subsurface study of the Middle Eocene Ainsa System, Spanish Pyrenees.
792 Sedimentology, **61**, 1298–1331.

793 **Henriksen, S., Pontén, A., Janbu, N.** and **Paasch, B.** (2011) The importance of sediment supply and
794 sequence-stacking pattern in creating hyperpycnal flows. In: Sediment Transfer from Shelf to Deep
795 Water - Revisiting the Delivery System (Eds R.M. Slatt and C. Zavala), AAPG Studies in Geology, **61**,
796 129-152.

797 **Herbert, C.T.** and **Compton, J.S.** (2007) Depositional environments of the lower Permian Dwyka
798 diamictite and Prince Albert shale inferred from the geochemistry of early diagenetic concretions,
799 southwest Karoo Basin, South Africa. Sed. Geol., **194**, 263–277.

800 **Hodgson, D.M., Flint, S.S., Hodgetts, D., Drinkwater, N.J., Johannessen, E.P.** and **Luthi, S.M.**
801 (2006) Stratigraphic evolution of fine-grained submarine fan systems, Tanqua Depocenter, Karoo Basin,
802 South Africa. J. Sed. Res., **76**, 20–40.

Hubbard, S.M., de Ruig, M.J. and **Graham, S.A.** (2009) Confined channel-levee complex development in an elongate depo-center: deep-water Tertiary strata of the Austrian Molasse basin. Mar. Petrol. Geol., **26**, 85–112.

Ichaso, A.A. and **Dalrymple, R.W.** (2009) Tide- and wave-generated fluid mud deposits in the Tilje Formation (Jurassic), offshore Norway. Geology, **37**, 539–542.

Isbell, J.L., Cole, D.I. and **Catuneanu, O.** (2008) Carboniferous-Permian glaciation in the main Karoo Basin, South Africa: stratigraphy, depositional controls, and glacial dynamics. Geol. Soc. Am. Spec. Pap., **441**, 71–82.

Jackson, A.M., Hasiotis, S.T. and **Flaig, P.P.** (2016) Ichnology of a paleopolar, river-dominated, shallow marine deltaic succession in the Mackellar Sea: The Mackellar Formation (Lower Permian), Central Transantarctic Mountains, Antarctica. Palaeogeogr. Palaeoclimatol. Palaeoecol., **441**, 266-291.

Johnson, S.D., Flint, S.S., Hinds, D. and **Wickens, H.d.V.** (2001) Anatomy, geometry and sequence stratigraphy of basin floor to slope turbidite systems, Tanqua Karoo, South Africa. Sedimentology, **48**, 987–1023.

Johnson, M.R., van Vuuren, C.J., Visser, J.N.J., Cole, D.I., Wickens, H.d.V., Christie, A.D.M., Roberts, D.L. and **Brandl, G.** (2006) Sedimentary rocks of the Karoo Supergroup. In: The Geology of South Africa (Eds M.R. Johnson, C.R. Anhaeusser and R.J. Thomas), pp. 461-499. Geological Society of South Africa and Council for Geoscience, Pretoria.

Kane, I.A. and **Pontén, A.S.M.** (2012) Submarine transitional flow deposits in the Paleogene Gulf of Mexico. Geology, **40**, 1119–1122.

Kane, I.A., Pontén, A.S.M., Vangdal, B., Eggenhuisen, J.T., Hodgson, D.M. and **Spychala, Y.T.** (2017) The stratigraphic record and processes of turbidity current transformation across deep-marine lobes. Sedimentology, **64**, 1236–1273.

Knapp, L.J., McMillan, J.M. and **Harris, N.B.** (2017) A depositional model for organic-rich Duvernay Formation mudstones. Sed. Geol., **347**, 160–182.

Knaust, D. and **Bromley, R.** (2012) Trace fossils as Indicators of Sedimentary Environments. Elsevier, Amsterdam, 960 pp.

Kneller, B. and **McCaffrey, W.D.** (2003) The interpretation of vertical sequences in turbidite beds: the influence of longitudinal flow structure. J. Sed. Res., **73**, 706–713.

Konitzer, S.F., Davies, S.J., Stephenson, M.H. and **Leng, M.J.** (2014) Depositional controls on mudstone lithofacies in a basinal setting: implications for the delivery of sedimentary organic matter. J. Sed. Res., **84**, 198–214.

Lazar, R.O., Bohacs, K.M., Macquaker, J.H.S., Schieber, J. and **Demko, T.M.** (2015) Capturing key attributes of fine-grained sedimentary rocks in outcrops, cores, and thin sections: nomenclature and description guidelines. J. Sed. Res., **85**, 230–246.

Li, Z. and **Schieber, J**. (2018) Detailled facies analysis of the Upper Cretaceous Tununk Shale Member, Henry Mountains Region, Utah: Implications for mudstone depositional models in epicontinental seas. Sed. Geol., **364**, 141-159.

López-Gamundi, O. and **Rossello, E.A.** (1998) Basin fill evolution and paleotectonic patterns along the Samfrau geosyncline: the Sauce Grande basin-Ventana foldbelt (Argentina) and Karoo basin-Cape foldbelt (South Africa) revisited. Geol. Rundsch., **86**, 819–834.

Loucks, R.G. and **Ruppel, S.C.** (2007) Mississippian Barnett Shale: lithofacies and depositional setting of a deep-water shale-gas succession in the Fort Worth Basin, Texas. AAPG Bull., **91**, 579–601.

Lowe, D.R. (1982) Sediment gravity flows: II, Depositional models with special reference to the deposits of high-density turbidity currents. J. Sed. Res., **52**, 279-297.

McCave, I.N., Manighetti, B. and **Robinson, S.G.** (1995) Sortable silt and fine sediment size/composition slicing: Parameters for palaeocurrent speed and palaeoceanography. Palaoceanography, **10**, 593-610.

MacEachern, J.A., Bann, K.L., Pemberton, G.S. and **Gingras, M.K.** (2007) The ichnofacies paradigm: high-resolution paleoenvironmental interpretation of the rock record. In: Applied Ichnology (Eds J.A. MacEachern, K.L. Bann, M.K. Gingras and S.G. Pemberton), SEPM Short Course Notes, 52, 27-64.

Macquaker, J.H.S. and **Taylor, K.G**. (1996) A sequence-stratigraphic interpretation of a mudstone-dominated succession: the Lower Jurassic Cleveland Ironstone Formation, UK. J. Geol. Soc. London, **153**, 759–770.

857 **Macquaker, J.H.S., Bentley, S.J.** and **Bohacs, K.M.** (2010) Wave-enhanced sediment-gravity flows
858 and mud dispersal across continental shelves: reappraising sediment transport processes operating in
859 ancient mudstone successions. Geology, **38**, 947–950.

860 **McLachlan, I.R.** and **Anderson, A.** (1973) A review of the evidence for marine conditions in southern
861 Africa during Dwyka times. Paleontologia africana, **15**, 37–64.

862 **McLachlan, I.R.** and **Jonker, J.P.** (1990) Tuff beds in the northwestern part of the Karoo Basin. S. Afr.
863 J. Geol., **93**, 329–338.

864 **Mitchum, R.M., Vail, P.R.** and **Thompson, S.** (1977) Seismic stratigraphy and global changes of sea
865 level, Part 2. The depositional sequence as a basic unit for stratigraphic analysis. In: Seismic
866 Stratigraphy - Applications to Hydrocarbon Exploration (Ed. C.E. Payton), Am. Assoc. Petrol. Geol.
867 Mem., **27**, 53-62.

868 **Mulder, T.** and **Syvitski, J.P.M.** (1995) Turbidity currents generated at river mouths during exceptional
869 discharges to the world oceans. J. Geol., **103**, 285–299.

870 **Mulder, T.** and **Syvitski, J.P.M.** (1996) Climatic and morphologic relationships of rivers: implications of
871 sea-level fluctuations on river loads. J. Geol., **104**, 509–523.

872 **Mulder, T**. and **Alexander, J.** (2001) The physical character of subaqueous sedimentary density flow
873 and their deposits. Sedimentology, **48,** 269-299.

874 **Mulder, T., Syvitski, J.P.M., Migeon, S., Faugères, J.C.** and **Savoye, B.** (2003) Marine hyperpycnal
875 flows: Initiation, behavior and related deposits. A review. Mar. Petrol. Geol., **20**, 861–882.

876 **Mutti, E.** (1977) Distinctive thin-bedded turbidites facies and related depositional environments in the
877 Eocene Hecho Group (South-central Pyrenees, Spain). Sedimentology, **24**, 107–131.

878 **Mutti, E.** (1985) Turbidite systems and their relations to depositional sequences. In: Provenance of
879 Arenites (Ed. G.G. Zuffa), pp. 65–93. Springer Netherlands, Dordrecht.

880 **Mutti, E.** and **Sonnino, M.** (1981) Compensation cycles: a diagnostic feature of turbidites sandstone
881 lobes, IAS 2nd Eur. Meet., Bologna, Italy, 120-123.

882 **Mutti, E.** and **Normark, W.R.** (1991) An integrated approach to the study of turbidite systems. In:

883 Seismic Facies and Sedimentary Processes of Submarine Fans and Turbidite System (Eds P. Weimer,
884 and M.H. Link), pp. 75–106. Springer, New York,.

885 **Mutti, E., Tinterri, R., Benevelli, G., di Biase, D.** and **Cavanna, G.** (2003) Deltaic, mixed and turbidite
886 sedimentation of ancient foreland basins. Mar. Pet. Geol., **20**, 733–755.

887 **Nakajima, T.** (2006) Hyperpycnites deposited 700 km away from river mouths in the Central Japan Sea.
888 J. Sed. Res., **76**, 60–73.

889 **Nemec, W.** (1995) The dynamics of deltaic suspension plumes. Geol. Deltas, 31–93.

890 **Newport, S.M., Jerrett, R.M., Taylor, K.G., Hough, E.** and **Worden, R.H**. (2018) Sedimentology and
891 microfacies of a mud-rich slope succession: in the Carboniferous Bowland Basin, NW England (UK). J.
892 Geol. Soc. London, **175**, 247–262.

893 **Petter, A.L.** and **Steel, R.J.** (2006) Hyperpycnal flow variability and slope organization on an Eocene
894 shelf margin, Central Basin, Spitsbergen. AAPG Bull., **90**, 1451–1472.

895 **Pettingill, H.S.** and **Weimer, P.** (2002) Worldwide deepwater exploration and production: past, present,
896 and future. Lead. Edge, **21**, 371–376.

897 **Pickering, K.T., Stow, D.A. V., Watson, M.** and **Hiscott, R.** (1986) Deep-water facies, processes and
898 models: a review and classification scheme for modern and ancient sediments. Earth-Sci. Rev., **23**, 75–
899 174.

900 **Pierce, C.S., Haughton, P.D.W., Shannon, P.M., Pulham, A.J., Barker, S.P.** and **Martinsen, O.J.**
901 (2018) Variable character and diverse origin of hybrid event beds in a sandy submarine fan system,
902 Pennsylvanian Ross Sandstone Formation, western Ireland. Sedimentology, **65**, 952–992.

903 **Plink-Bjölrklund, P.** and **Steel, R.J.** (2004) Initiation of turbidity currents: outcrop evidence for Eocene
904 hyperpycnal flow turbidites. Sed. Geol., **165**, 29–52.

905 **Plint, G.A.** (2014) Mud dispersal across a Cretaceous prodelta: storm-generated, wave-enhanced
906 sediment gravity flows inferred from mudstone microtexture and microfacies. Sedimentology, **61**, 609–
907 647.

908 **Plint, A.G.** and **Macquaker, J.H.S**. (2013) Bedload transport of mud across a wide, storm-influenced

909 ramp: Cenomanian-Turonian Kaskapau Formation, Western Canada foreland basin-Reply. J. Sed.
910 Res., **83**, 1200-1201.

911 **Plint, G.A., Macquaker, J.H.S.** and **Varban, B.L.** (2012) Bedload transport of mud across a wide,
912 storm-influenced ramp: Cenomanian-Turonian Kaskapau Formation, Western Canada Foreland Basin.
913 J. Sed. Res., **82**, 801–822.

914

915 **Posamentier, H.W., Erskine, R.D.** and **Mitchum, R.M.** (1991) Models for submarine-fan deposition
916 within a sequence-stratigraphic framework. In: Seismic Facies and Sedimentary Processes of
917 Submarine Fans and Turbidite Systems (Eds P. Weimer and M.H Link), pp. 127-136. Springer, New
918 York.

919 **Posamentier, H.W**. and **Kolla, V**. (2003) Seismic geomoprhology and stratigraphy of depositional
920 elements in deep-water settings. J. Sed. Res., **73**, 367-388.

921 **Poyatos-Moré, M., Jones, G.D., Brunt, R.L., Hodgson, D.M., Wild, R.J.** and **Flint, S.S.** (2016) Mud-
922 dominated basin-margin progradation: processes and implications. J. Sed. Res., **86**, 863–878.

923 **Pysklywec, R.N.** and **Mitrovica, J.X**. (1999) The role of subduction-induced subsidence in the evolution
924 of the Karoo Basin. J. Geol., **107**, 155–164.

925 **Scheffler, K., Hoernes, S.** and **Schwark, L.** (2003) Global changes during Carboniferous-Permian
926 glaciation of Gondwana: linking polar and equatorial climate evolution by geochemical proxies. Geology,
927 **31**, 605–608.

928 **Scheffler, K., Buehmann, D.** and **Schwark,** L. (2006) Analysis of late Palaeozoic glacial to postglacial
929 sedimentary successions in South Africa by geochemical proxies - Response to climate evolution and
930 sedimentary environment. Palaeogeogr. Palaeoclimatol. Palaeoecol., **240** 184–203.

931 **Schieber, J.** (1994) Evidence for high-energy events and shallow-water deposition in the Chattanooga
932 Shale, Devonian, central Tennessee, USA. Sed. Geol., **93**, 193–208.

933 **Schieber, J.** (1998) Sedimentary features indicating erosion, condensation, and hiatuses in the
934 Chattanooga Shale of Central Tennessee: relevance for sedimentary and stratigraphic evolution. In:
935 Shales and Mudstones I: Basin Studies, Sedimentology and Paleontology (Eds J. Schieber, W.

936 Zimmerle and P.S. Sethi), pp. 187-215. E. Schweizerbart'sche Verlagsbuchhandlung (Nagele u.
937 Obermiller), Stuttgart.

938 **Schieber, J.** (1999) Distribution and deposition of mudstone facies in the Upper Devonian Sonyea
939 Group of New York. J. Sed. Res., **69**, 909–925.

940 **Schieber, J.** (2016) Experimental testing of the transport-durability of shale lithics and its implications
941 for interpreting the rock record. Sed. Geol., **331**, 162–169.

942 **Schieber, J.** and **Southard, J.B.** (2009) Bedload transport of mud by floccule ripples - Direct
943 observation of ripple migration processes and their implications. Geology, **37**, 483–486.

944 **Schieber, J.,** and **Bennett, R.** (2013) Bedload transport of mud across a wide, storm-influenced ramp:
945 Cenomanian-Turonian Kaskapau Formation, Western Canada Foreland Basin-Discussion. J. Sed. R.,
946 **83**, 1198-1199.

947 **Schieber, J., Southard, J.B.** and **Thaisen, K.** (2007) Accretion of mudstone beds from migrating
948 floccule ripples. Science, **318**, 1760–1763.

949 **Schieber, J., Southard, J.B.** and **Schimmelmann, A.** (2010) Lenticular shale fabrics resulting from
950 intermittent erosion of water-rich muds--interpreting the rock record in the light of recent flume
951 experiments. J. Sed. Res., **80**, 119–128.

952 **Scholle, P.A.** (1971) Sedimentology of fine-grained deep-water carbonate turbidites, Monte Antola
953 Flysch (upper cretaceous), Northern Apennines, Italy. Geol. Soc. Am. Bull., **82**, 629–658.

954 **Shanmugam, G., Moiola, R.J.** and **Damuth, J.E**. (1985) Eustatic control of submarine fan
955 development. In: Submarine Fans and Related Turbidite Systems (Eds A.H. Bouma, W.R. Normark and
956 N.E. Barnes), pp. 23–28. Springer, New York.

957 **Shanmugam, G.** (2006) Deep-water processes and facies models: Implications for sandstone
958 petroleum reservoirs. Elsevier.

959 **Smith, R.M.H.** (1990) A review of stratigraphy and sedimentary environments of the Karoo Basin of
960 South Africa. J. Afr. Earth Sci., **10**, 117–137.

961 **Southern, S.J., Kane, I.A., Warchoł, M.J., Porten, K.W.** and **McCaffrey, W.D.** (2017) Hybrid event

962 beds dominated by transitional-flow facies: character, distribution and significance in the maastrichtian
963 springar formation, north-west vøring basin, Norwegian Sea. Sedimentology, **64**, 747–776.

964 **Soyinka, O.A.** and **Slatt, R.M.** (2008) Identification and micro-stratigraphy of hyperpycnites and
965 turbidites in Cretaceous Lewis Shale, Wyoming. Sedimentology, **55**, 1117–1133.

966 **Spychala, Y.T., Hodgson, D.M., Prélat, A., Kane, I.A., Flint, S.S**. and **Mountney, N.P.** (2017) Frontal
967 and lateral submarine lobe fringes: Comparing sedimentary facies, architecture and flow processes. J.
968 Sed. Res., **87**, 75-96.

969 **Stow, D.A.V.** and **Shanmugam, G.** (1980) Sequence of structures in fine-grained turbidites:
970 Comparison of recent deep-sea and ancient flysch sediments. Sed. Geol., **25**, 23–42.

971 **Stow, D.A.V.** and **Piper, D.J.W.** (1984) Deep-water fine-grained sediments: facies models. In: Fine
972 Grained Sediments: Deep-Water Processes and Facies (Eds D.A.V. Stow and D.J.W. Piper), Geol. Soc.
973 Spec. Publ., **15**, 611-646.

974 **Sumner, E.J., Talling, P.J.** and **Amy, L.A.** (2009) Deposits of flows transitional between turbidity
975 current and debris flow. Geology, **37**, 991–994.

976 **Talling, P.J., Masson, D.G., Sumner, E.J.** and **Malgesini, G.** (2012) Subaqueous sediment density
977 flows: depositional processes and deposit types. Sedimentology, **59**, 1937–2003.

978 **Talling, P.J., Paull, C.K**. and **Piper, D.J.W.** (2013) How are subaqueous sediment density flows
979 triggered, what is their internal structure and how does it evolve? Direct observations from monitoring of
980 active flows. Earth-Sci. Rev., **125**, 244–287.

981 **Tankard, A., Welsink, H., Aukes, P., Newton, R.** and **Stettler, E.** (2009) Tectonic evolution of the Cape
982 and Karoo basins of South Africa. Mar. Petrol. Geol., **26**, 1379–1412.

983 **Taylor, A.M.** and **Goldring, R.** (1993) Description and analysis of bioturbation and ichnofabric. J. Geol.
984 Soc. London, **150**, 141–148.

985 **Taylor, K.G.** and **Curtis, C.D.** (1995) Stability and facies association of early diagnetic mineral
986 assemblages: an example from a Jurassic ironstone-mudstone succession, UK. J. Sed. Res., **65**, 358-
987 368.

Theron, J.N. and **Blignault, H.J.** (1975) A model for the sedimentation of the Dwyka glacials in the southwestern Cape. Gondwana Geol., 347–356.

Trabucho-Alexandre, J., Dirkx, R., Veld, H., Klaver, G and **de Boer, P.L**. (2012) Toarcian black shales in the Dutch Central Graben: Record of energetic, variable depositional conditions during an oceanic anoxic event. J. Sed. Res., **82**, 104-120.

Van der Kolk, D.A., Flaig, P.P. and **Hasiotis, S.T**. (2015) Paleoenvironmental reconstruction of a late Cretaceous, muddy, river-dominated polar deltaic system: Schrader Bluff-Prince Creek Formation Transition, Shivugak Bluffs, North Slope of Alaska, U.S.A. J. Sed. Res., **85**, 903-936.

Van Lente, B. (2004) Chemostratigraphic trends and provenance of the Permian Tanqua and Laingsburg depocentres, southwestern Karoo Basin, South Africa. Unpublished PhD thesis, University of Stelenbosch, South Africa, 339 pp.

Van der Merwe, W.C., Flint, S.S. and **Hodgson, D.M.** (2010) Sequence stratigraphy of an argillaceous, deepwater basin-plain succession: Vischkuil Formation (Permian), Karoo Basin, South Africa. Mar. Petrol. Geol., **27**, 321–333.

Veevers, J.J., Cole, D.I. and **Cowan, E.J.** (1994) Southern Africa: Karoo Basin and Cape Fold Belt. In: Permian-Triassic Pangean Basins and foldbelts along the Panthalassan margin of Gondwanaland: Geological Society America, Memoir 184 (Eds J.J. Veevers and C.M. Powell), pp. 223-279. The Geological Society of America, Boulder, CO.

Viglietti, P.A., Rubidge, B.S. and **Smith, R.M.** (2017) New Late Permian tectonic model for South Africa's Karoo Basin: foreland tectonics and climate change before the end-Permian crisis. Scient. rep, **7**(1).

Viljoen, J.H.A. (1994) Sedimentology of the Collingham Formation, Karoo Supergroup. S. Afr. J. Geol., **97**, 167–183.

Viljoen, J.H.A. (2005) Tierberg Formation. SA committe for stratigraphy, Catalogue of South African Lithostratigraphic units, **8**, 37–40.

Visser, J.N.J. (1992) Deposition of the early to late Permian Whitehill Formation during a sea-level highstand in a juvenile foreland basin. S. Afr. J. Geol., **95**, 181–193.

1015 **Visser, J.N.J.** (1994) A Permian argillaceous syn- to post-glacial foreland sequence in the Karoo Basin,
1016 South Africa. *Earth's Glac. Rec.*, **1**, 193–203.

1017 **Visser, J.N.J.** and **Praekelt, H.E.** (1996) Subduction, mega-shear systems and Late Palaeozoic basin
1018 development in the African segment of Gondwana. Geol. Rundsch., **85**, 632–646.

1019 **Visser, J.N.J.** (1997) Deglaciation sequences in the Permo-Carboniferous Karoo and Kalahari basins
1020 of southern Africa: a tool in the analysis of cyclic glaciomarine basin fills. Sedimentology, **44**, 507–521.

1021 **Weimer, P., Pettingill, H.S.** and **Nilsen, T.H.** (2007) Global overview of deep-water exploration and
1022 production. In: Atlas of Deep-water Outcrops. American Association of Petroleum Geologists Studies in
1023 Geology, **56**, 7–11.

1024 **Wetzel, A.** (1991) Ecologic interpretation of deep-sea trace fossil communities. Palaeogeogr.
1025 Palaeoclimatol. Palaeoecol., **85**, 47-69.

1026 **Wickens, H.d.V.** (1994) Basin floor fan building turbidites of the southwestern Karoo Basin, Permian
1027 Ecca Group, South Africa. Unpublished PhD thesis, University of Port Elizabeth, Port Elizabeth (South
1028 Africa), 233 pp.

1029 **Wignall, P.B**. (1994) Black Shales. Oxford University Press, Oxford. 124 pp.

1030 **Wild, R.J., Flint, S.S.** and **Hodgson, D.M.** (2009) Stratigraphic evolution of the upper slope and shelf
1031 edge in the Karoo Basin, South Africa. Basin Res., **21**, 502–527.

1032 **Wilson, R.D.** and **Schieber, J.** (2015) Sedimentary facies and depositional environment of the Middle
1033 Devonian Geneseo Formation of New York, U.S.A. J. Sed. Res., **85**, 1393–1415.

1034 **Wynn, R.B., Masson, D.G., Stow, D.A.V**. and **Weaver, P.P.E.** (2000) The Northwest African slope
1035 apron: a modern analogue for deep water systems with complex seafoor topography. Mar. Petrol. Geol.,
1036 **17**, 253–265.

1037 **Zavala, C., Arcuri, M., Di Meglio, M., Diaz, H.G.** and **Contreras, C.** (2011) A genetic facies tract for
1038 the analysis of sustained hyperpycnal flow deposits. AAPG Studies in Geology, **61**, 31–52.

1039 **Zavala, C., Arcuri, M.** and **Blanco Valiente, L.** (2012) The importance of plant remains as diagnostic
1040 criteria for the recognition of ancient hyperpycnites. Rev. Paléobiol., **11**, 457–469.

Figure captions

Fig. 1. Study area. (A) Satellite view of southwest South Africa with location of study area (Tanqua depocentre) indicated by white square. (B) Satellite view of Tanqua depocentre situated along eastern side of N–S Cederberg Branch of the Cape Fold Belt. Black square indicates location of zoomed map. Red dot indicates location of OR-01 core presented in this study. (C) Schematic stratigraphic log of Karoo Supergroup in Tanqua depocentre with stratigraphic extent of core presented in this study indicated by red dotted square. Adapted from Wickens (1994).

Fig. 2. Summarized sedimentary log of the OR-01 core (from 948.5 m to 410 m), including facies, bioturbation intensity, tilted intervals, pyrites nodules, concretions and thin section locations. Dotted lines in ash column indicate where an ash bed is not preserved in core but ash material was recovered during drilling. See Fig. 1 for geographical location. Bioturbation intensity scale from Taylor and Goldring (1993). The Tierberg Formation has been subdivided into three parts based on variations in depositional units stacking pattern. fm = fine mudstone, cm = coarse mudstone.

Fig. 3. Illustrations of the nine facies identified in OR-01 core. White dotted squares in core views indicate locations of thin-section views. White dotted squares in thin-section views indicate locations of optical microscope views. **Facies 1:** very thin-bedded mudstone. (A) Dry core photograph (641.60 m). (B) Thin-section scan. Erosional beds, normally graded or inversely-to-normally graded and characterized by planar-parallel laminations. Detailed sedimentary log of thin section presented in Fig. 4A. (C) Optical microscope photograph. Coarse mudstone dominated by quartz (Q) and clay. Common wood fragments (WF) and micas (M). **Facies 2**: mottled very thin-bedded mudstone. (D) Dry core photograph (753.65 m). Beds usually discontinuous. (E) Thin-section scan. Erosional beds with laminations rarely preserved (yellow arrows). (F) Optical microscope photograph. Texture similar to F1. Potential mudstone intraclast (yellow-dotted line). **Facies 3**: intraclast-bearing thin-bedded to medium-bedded mudstone. (G) Dry core photograph (508.80 m). Erosional dark grey medium mudstone bed overlying partially cemented mudstone (F7). Pebble-sized mudstone intraclasts located in basal part of bed (yellow-dotted lines). (H) Thin-section scan. Erosional contact. Note stringer-type texture of mudstone intraclast and pyrite aggregate above basal erosional surface. (I) Optical microscope photograph. Poorly sorted texture

dominated by quartz (Q) floating in matrix of clay and wood fragments (WF). Note medium sand-sized intraclast (yellow-dotted lines). **Facies 4**: intraclast-bearing, very thin-bedded to thin-bedded mudstone. (J) Dry core photograph (609.90 m). Bed boundaries usually faint and hard to spot at core scale. (K) Thin-section scan. Two bioturbated beds recognized in upper part without clear grading (bed bases indicated by yellow arrows). (L) Optical microscope photograph. Coarse mudstone. Dominance of quartz (Q) and clay. Common wood fragments (WF). Note fine sand-sized mudstone intraclast (yellow dotted lines). **Facies 5**: homogenous mudstone. (M) Dry core photograph (486.40 m). Fine to coarse mudstone. No physical sedimentary structures recognized due to intense bioturbation. (N) Thin-section scan. Mottled texture. (O) Optical microscope photograph. Texture consists of dominance of quartz (Q), clay and wood fragments (WF). Note medium sand-sized intraclast (yellow dotted line). **Facies 6**: carbonaceous mudstone. (P) Dry core photograph (930.54 m). Dark grey coarse mudstone, structureless at core scale. (Q) Thin-section scan. Subtle bed contacts (yellow arrows). White arrows indicate remnant low-angle to planar-parallel laminations. (R) Optical microscope photograph. Texture dominated by quartz floating in matrix of wood fragments and clays. Note fine sand-sized feldspar grain. **Facies 7**: partially cemented mudstone. (S) Dry core photograph (782.85 m). Intensely bioturbated cemented mudstone. (T) Thin-section scan. (U) Optical microscope photograph. Cement consists of calcium carbonate and calcium phosphate. **Facies 8**: deformed deposits. (V) Dry core photograph (725.60 m) showing base of lower deformed interval. Base indicated by white-dotted line. Note presence of mudstone intraclasts (yellow arrows) and similar texture observed in F3. (W) Dry core photograph (723.50 m) showing internal deformation of lower deformed interval. Note overturned strata below ash-rich sandstone block as well as the soft-sediment deformation into ash-rich sandstone bed. (X) Dry core photograph (711.70 m) showing internal deformations of middle deformed interval. Note combination of plastic and brittle deformation. (Y) Dry core photograph (593.30 m) showing internal deformations of upper deformed interval. Note combination of plastic and brittle deformation. **Facies 9**: ash-rich sandstone. (Z) Wet core photograph (552.20 m). Sharp-based, normally graded, ash-rich, very fine-grained sandstone bed. Lower part characterized by planar-parallel to low-angle laminated very fine sandstone passing upward into bioturbated, structureless to deformed very fine sandstone with carbonate cemented top. Sharp contact between the very fine sandstone and bioturbated (Helminthopsis) coarse mudstone (mud cap) is present.

Fig. 4. Facies 1 (very thin-bedded mudstone): examples of key features. (A) Wet core photograph

(700.15 m). Fine to coarse mudstone with continuous mm-thick normally graded, inversely graded or inversely-to-normally graded beds. Bioturbation dominated by Helminthopsis (He) and Phycosiphon (Ph). (B) Wet core photograph (771.92 m). Scour (black dotted line) with coarse sand-sized mudstone clasts (white arrows). Carbonate-cemented bed with pyrite nodule located above scour. Bioturbation dominated by Helminthopsis (He). (C) Wet core photograph (620.80 m). Soft-sediment deformation. Black dotted lines indicate planes of deformation. (D) Optical microscope photograph (641.60 m). Example of bed type I. Erosional basal contact (black dotted line); lower subdivision (1) coarse mudstone with discontinuous planar-parallel laminations (yellow arrows indicate laminae); middle subdivision (2) structureless and normally graded coarse mudstone; upper subdivision (3) sharp-based ungraded bioturbated fine mudstone. (E) Optical microscope photograph (619.64 m). Example of bed type II. Gradational basal contact (black dotted line); lower subdivision (1) inversely graded fine to coarse mudstone with continuous planar-parallel laminations (yellow arrows indicate laminae); middle subdivision (2) structureless and normally graded fine to coarse mudstone; upper subdivision (3) sharp-base ungraded fine bioturbated mudstone. (F) BSE SEM image (641.60 m). Coarse mudstone, siliceous-argillaceous. Common wood fragments. Common quartz (Q) with minor mica (M), pyrite (Py) and feldspar.

Fig. 5. Facies 1 (very thin-bedded mudstone) microstratigraphy. Bed types (I or II) indicated close to graphic log. Note dominance of bed type I in the two examples. (A) Dry core photograph (left) and thin section scan (right) (641.60 m). Note complex microstratigraphy and pervasive presence of small burrows (mainly Helminthopsis and Phycosiphon). (B) Dry core photograph (left) and thin section scan (right) (814.70 m). Note soft-sediment deformations in thick bed at 1.6 cm. fm = fine mudstone; cm = coarse mudstone.

Fig. 6. Facies 3 (Intraclast-bearing thin- to medium-bedded mudstone) example of key features. (A) Wet core photograph (825.73 m). Intraclast-bearing, ungraded coarse mudstone. Largest intraclasts concentrated in lower part of bed (yellow arrows). Middle part of bed characterized by structureless coarse mudstone with smaller intraclasts. Upper part more pervasively bioturbated (Helminthopsis). Underlying partially cemented mudstone (F7) characterized by Conichnus (Co). Note similar texture between the mudstone intraclasts and the underlying cemented mudstone facies (B) Wet core photograph (500.74 m) of intraclast-bearing coarse mudstone. Intraclasts aligned along coarser grained

horizons. (C) Optical microscope photograph (500.74 m). Close-up view of intraclasts presented in (B). Intraclasts highly variable in size (from 80 µm to 700 µm long). Matrix dominated by mixture of quartz, feldspar, clay, and wood fragment. (D) Optical microscope photograph (500.74 m). Close-up view of texture of intraclasts.

Fig. 7. Facies 4 (intraclast-bearing very thin to thin-bedded mudstone) examples of key features. (A) Wet core photograph (568.34 m). Coarse-grained mudstone beds. Beds with two subdivisions: (i) normally graded coarse mudstone; and (ii) ungraded intraclast-bearing coarse mudstone (intraclasts indicated by yellow arrows). (B) Wet core photograph (665.15 m) of faintly bedded coarse mudstone. Note brown banding and laminae (white arrows). (C) Optical microscope photograph (946.58 m) of argillaceous-siliceous coarse mudstone. Note very fine sand-sized intraclast (yellow-dotted lines). (D) Optical microscope photograph (672.41 m) of poorly sorted argillaceous-siliceous coarse mudstone. Note intraclasts (yellow-dotted lines) and very fine sand-sized quartz (Q). (E) BSE-SEM image (672.41 m). Close-up view of an intraclast partially cemented by calcium phosphate and calcium carbonate in a matrix dominated by quartz and clay. (F) BSE-SEM image (672.41 m). Close-up view of calcium phosphate-rich elongated fragment, with internal structure, interpreted as a reworked bone fragment.

Fig. 8. Facies 8 (deformed deposits) examples of key features. Some deformations have been highlighted by black lines. (A) Dry core photograph of the lower deformed interval (from 725.50 to 718.90 m). Deformed interval bounded by white dotted lines. Dominance of plastic deformation (soft-sediment folding, liquefaction and sand injections). Note presence of decimetre thick, ash-rich sandstone blocks. (B) Dry core photograph of the middle-deformed interval (from 714.50 to 709.50 m). Base indicated by white dotted line. Plastic and brittle deformation. Plastic deformation consists of soft-sediment folding, liquefaction and sand injectites. Brittle deformation consists of normal faults (mainly listric) and reverse faults.

Fig. 9. Wet core photographs of trace fossils encountered in OR-01 succession. (A) Phycosiphon in F7 (555 m). (B) Helminthopsis in F1 (668.57 m). (C) Conichnus in F2 (743.70 m). (D) Planolites in F1 (695.31 m). (E) Thalassinoides in F2 (948.40 m). (F) Cosmorhaphe in F2 (847.90 m). (G) Chondrites in F2 (701 m). (H) Teichichnus in F5 (429 m). Note the different scales of the illustrations.

Fig. 10. Example of a deep-water mudstone depositional unit (from 646.15 to 628.65 m). See Fig. 2 for stratigraphic position. Note vertical transition from dominance of F1 to dominance of F2 and F4 as

observed in other depositional units in rest of succession. Facies transition accompanied with increase of bioturbation intensity and TOC. Bioturbation intensity scale from Taylor and Goldring (1993).

Fig. 11. Depositional model of Lower Ecca Group in southwest Karoo Basin. Low-density turbidity currents predominant near the sediment entry point (depositing F1 and F2), whereas debris flows and transitional flows predominant in a lateral or distal position (depositing F3, F4, F5 and F6). Early cementation processes (F7) in areas of low sediment accumulation rate in lateral or distal position.

Fig. 12. Summary conceptual schematic of deep-water mudstone depositional unit. Bed expressions of different facies illustrated. Bioturbation intensity scale from Taylor and Goldring (1993).

Fig. 13. Interpreted depositional processes depositing deep-water mudstones in the Lower Ecca Group of the southwest Karoo Basin. (A) In lower part of depositional units, depositional processes dominated by river-derived, dilute, low-density turbidity currents (hyperpycnal flows). Normally graded bed type I interpreted to represent distal expression of inversely-to-normally graded bed type II. (B) In upper part of depositional units in a lateral or distal position relative to the sediment input, depositional processes dominated by debris flows and transitional flows. Blue colour indicates early cementation and consolidation of the mud at the sea floor.

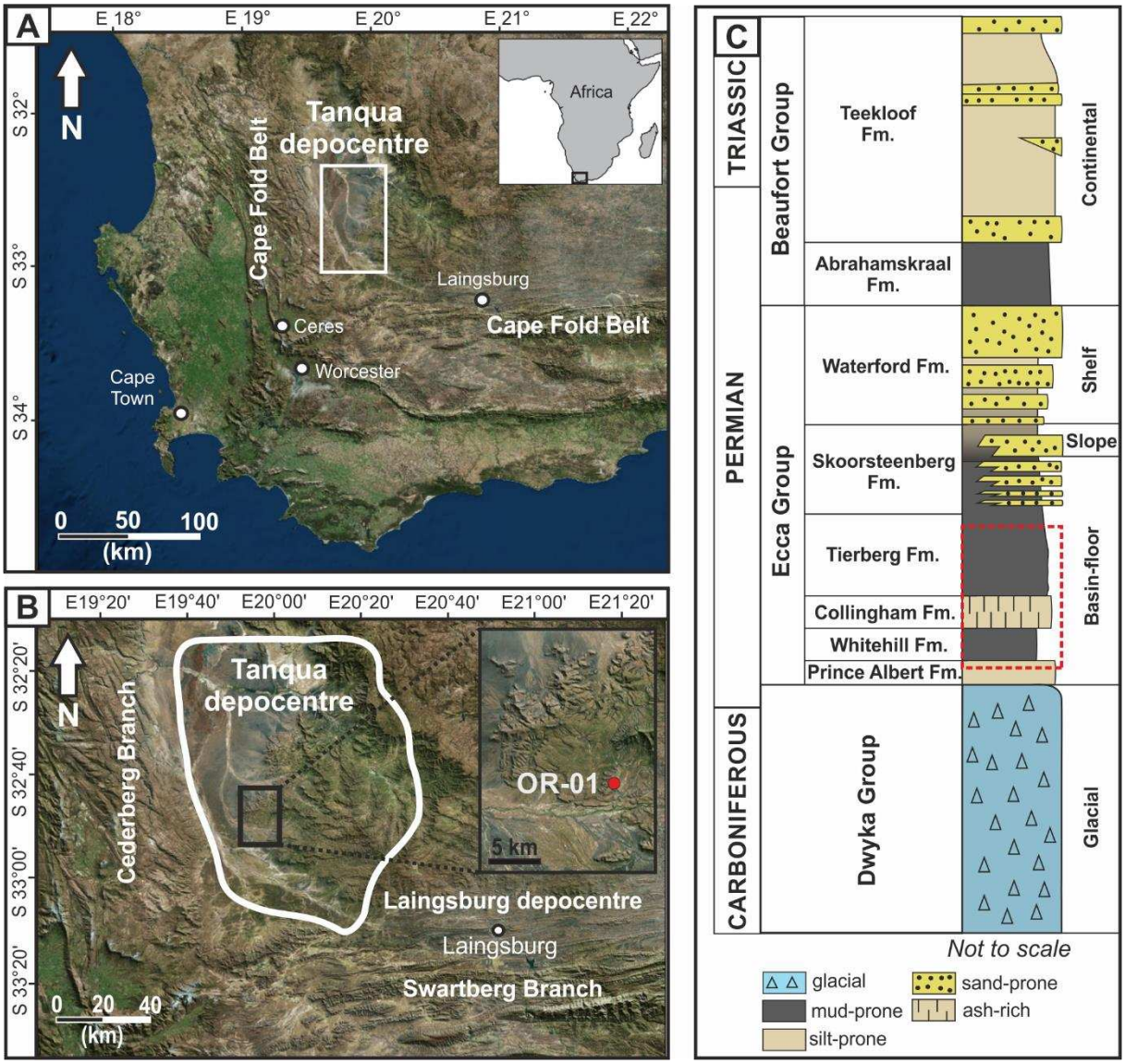
A
E 18°
E 19°
E 20°
E 21°
E 22°
S 32°
S 33°
S 34°
N
Africa
Tanqua depocentre
Cape Fold Belt
Laingsburg
Ceres
Cape Fold Belt
Worcester
Cape Town
0 50 100
(km)
B
E19°20'
E19°40'
E20°00'
E20°20'
E20°40'
E21°00'
E21°20'
S 32°20'
S 32°40'
S 33°00'
S 33°20'
N
Tanqua depocentre
Cederberg Branch
OR-01
5 km
Laingsburg depocentre
Laingsburg
Swartberg Branch
0 20 40
(km)
C
TRIASSIC
PERMIAN
CARBONIFEROUS
Beaufort Group
Ecca Group
Dwyka Group
Teekloof Fm.
Abrahamskraal Fm.
Waterford Fm.
Skoorsteenberg Fm.
Tierberg Fm.
Collingham Fm.
Whitehill Fm.
Prince Albert Fm.
Continental
Shelf
Slope
Basin-floor
Glacial
Not to scale
glacial
mud-prone
silt-prone
sand-prone
ash-rich

Figure 1

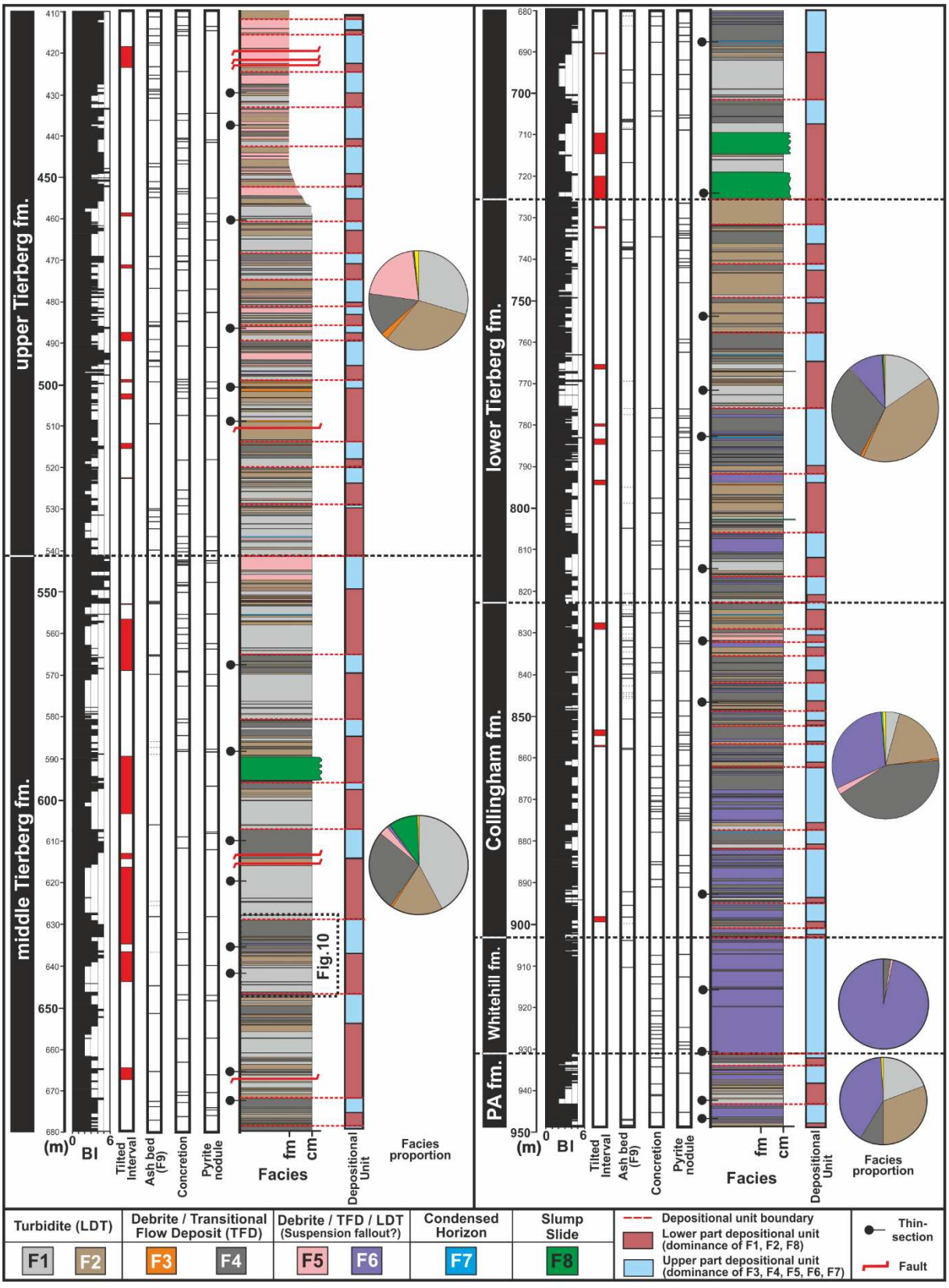

1176

1177 **Figure 2**

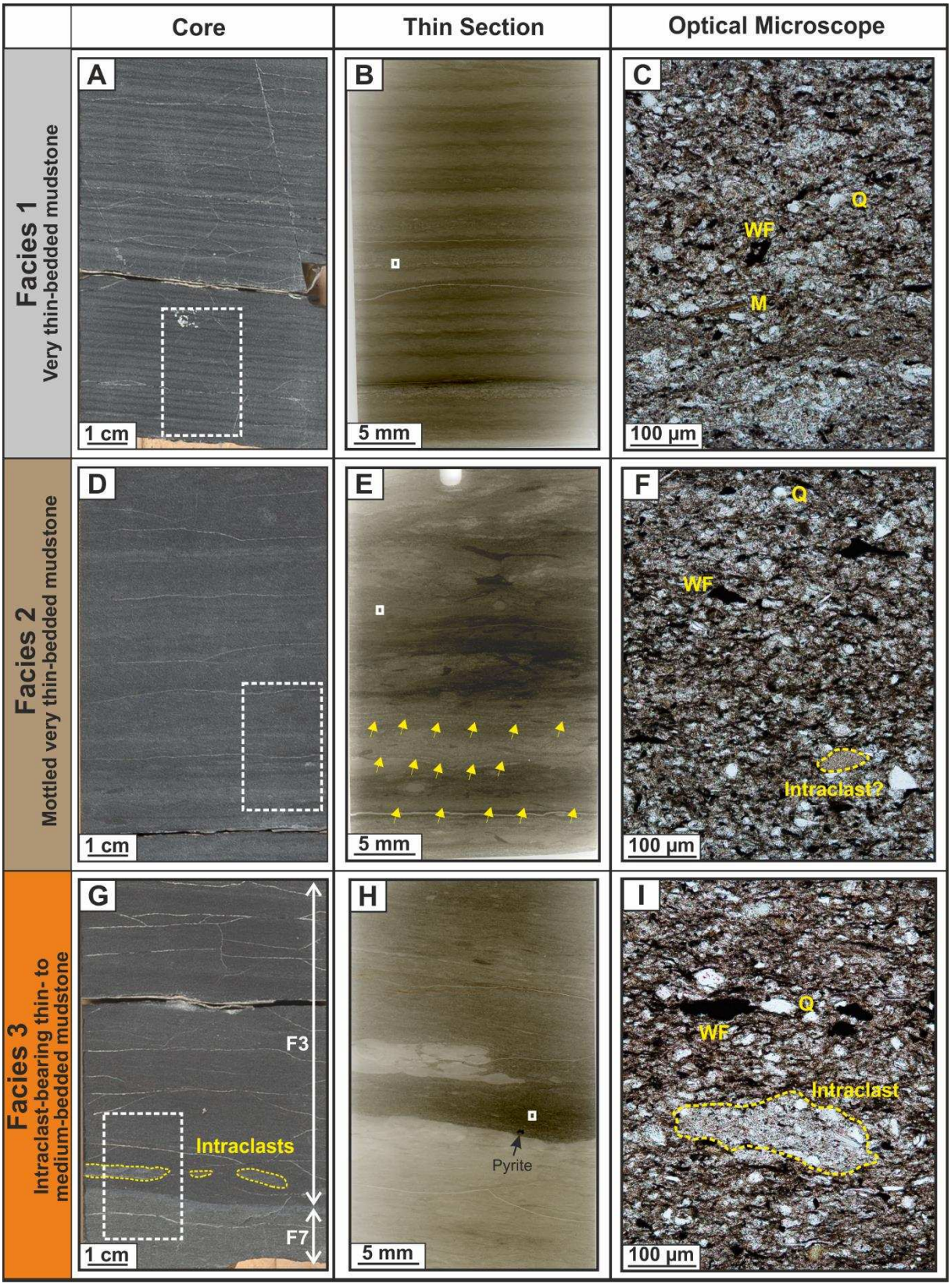

1178

1179 **Figure 3 (part 1)**

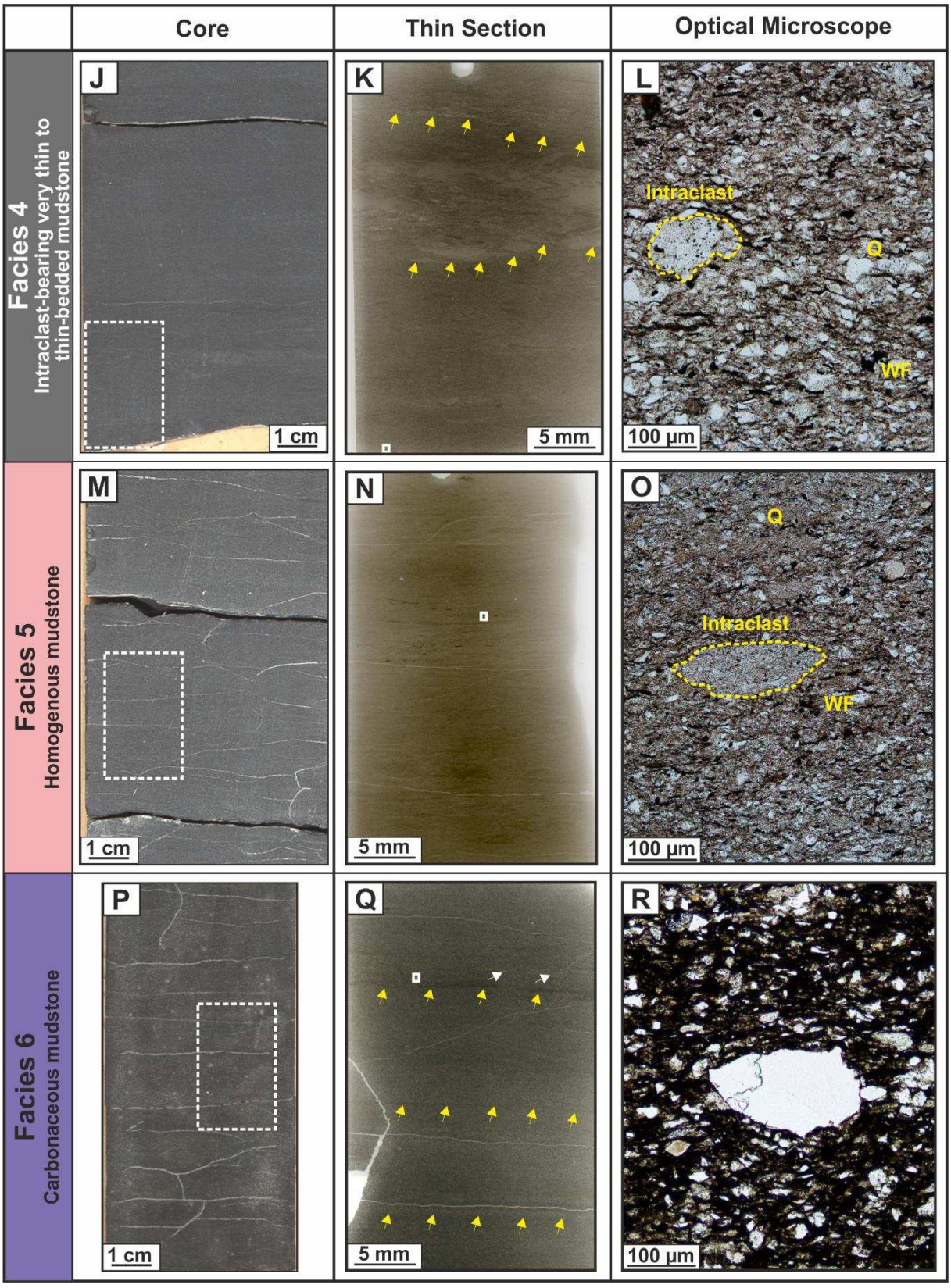

1180

1181 **Figure 3 (part 2)**

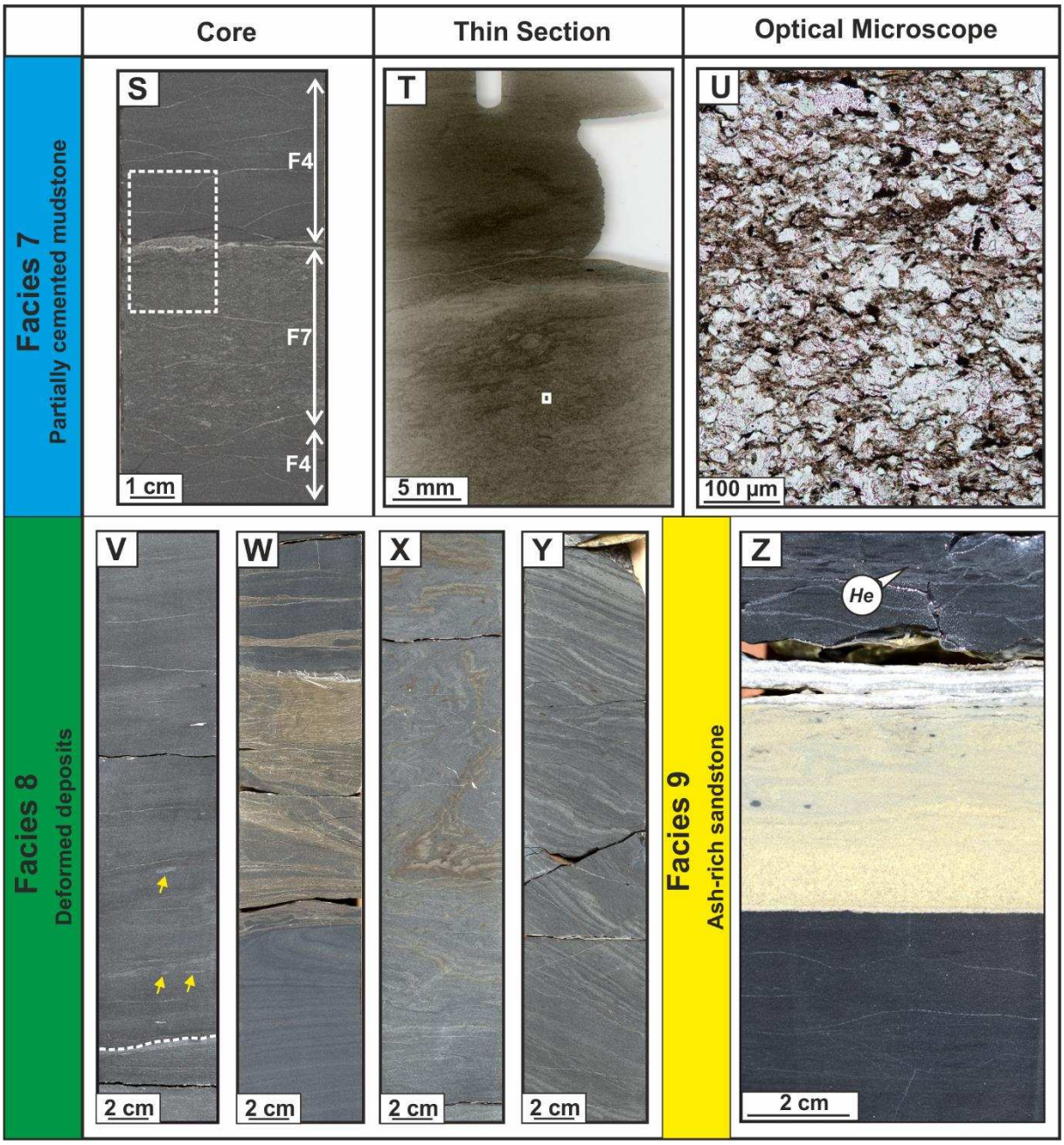

1182

1183 **Figure 3 (part 3)**

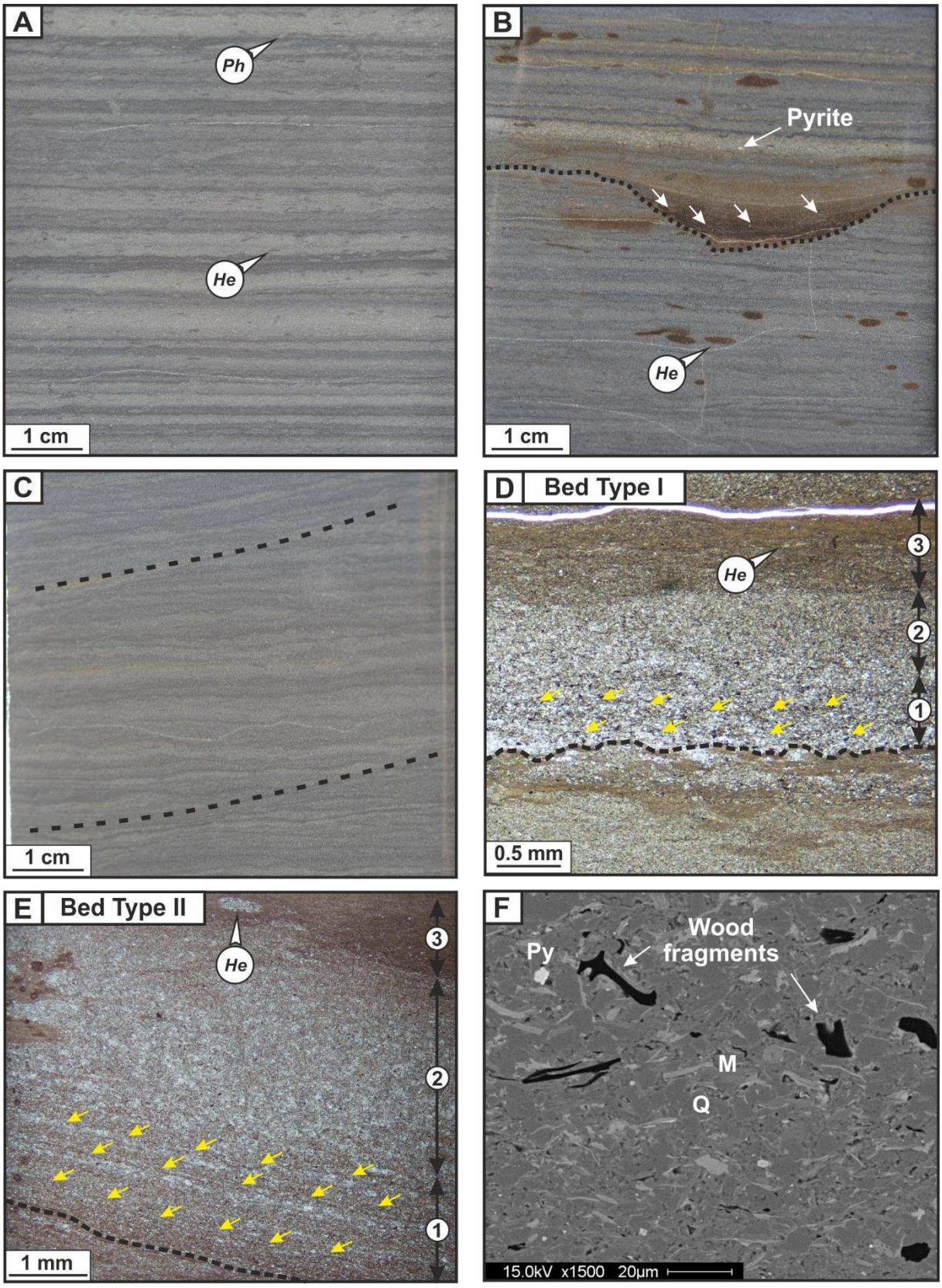

1184

1185 **Figure 4**

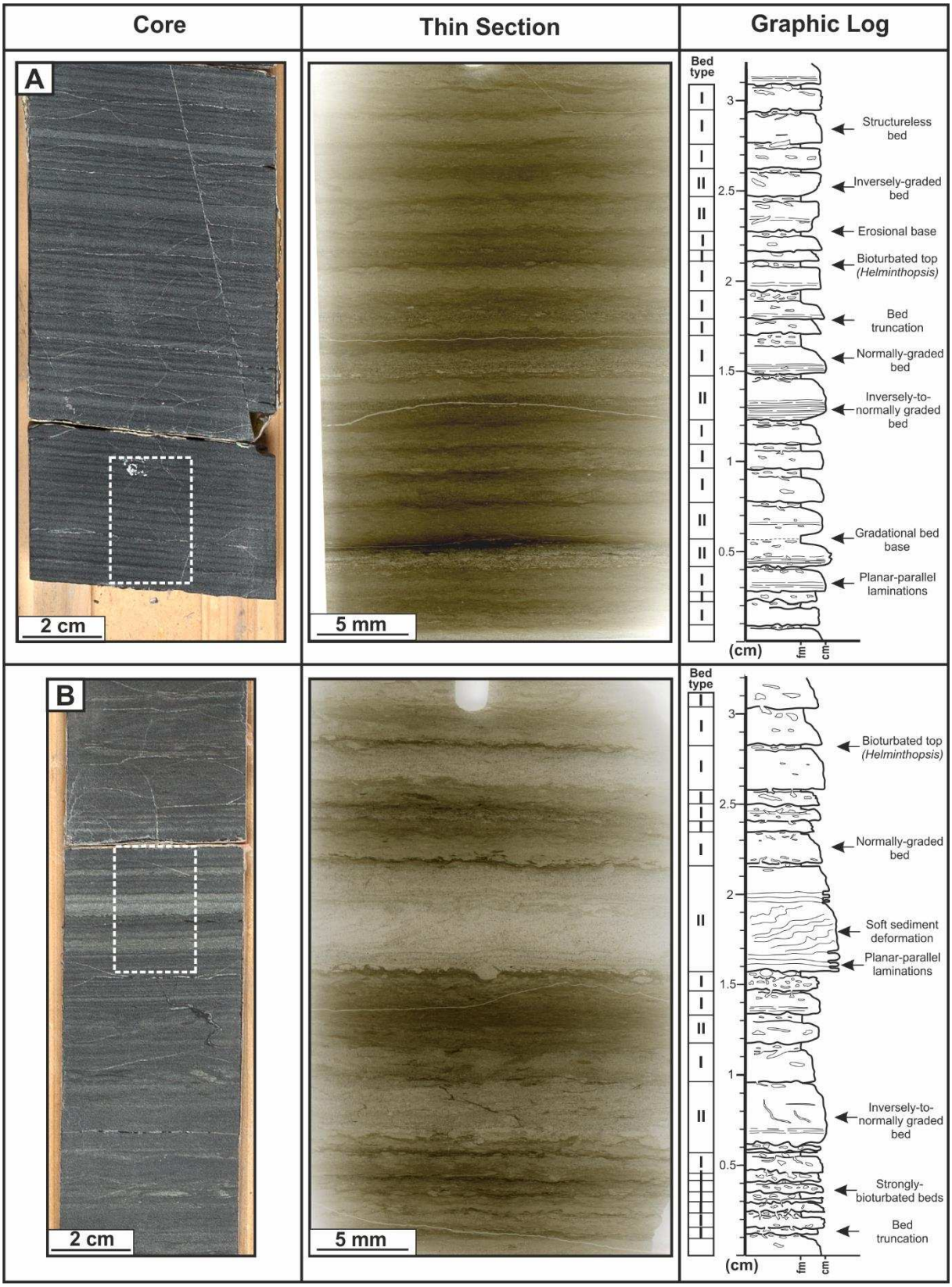

1186

1187 **Figure 5**

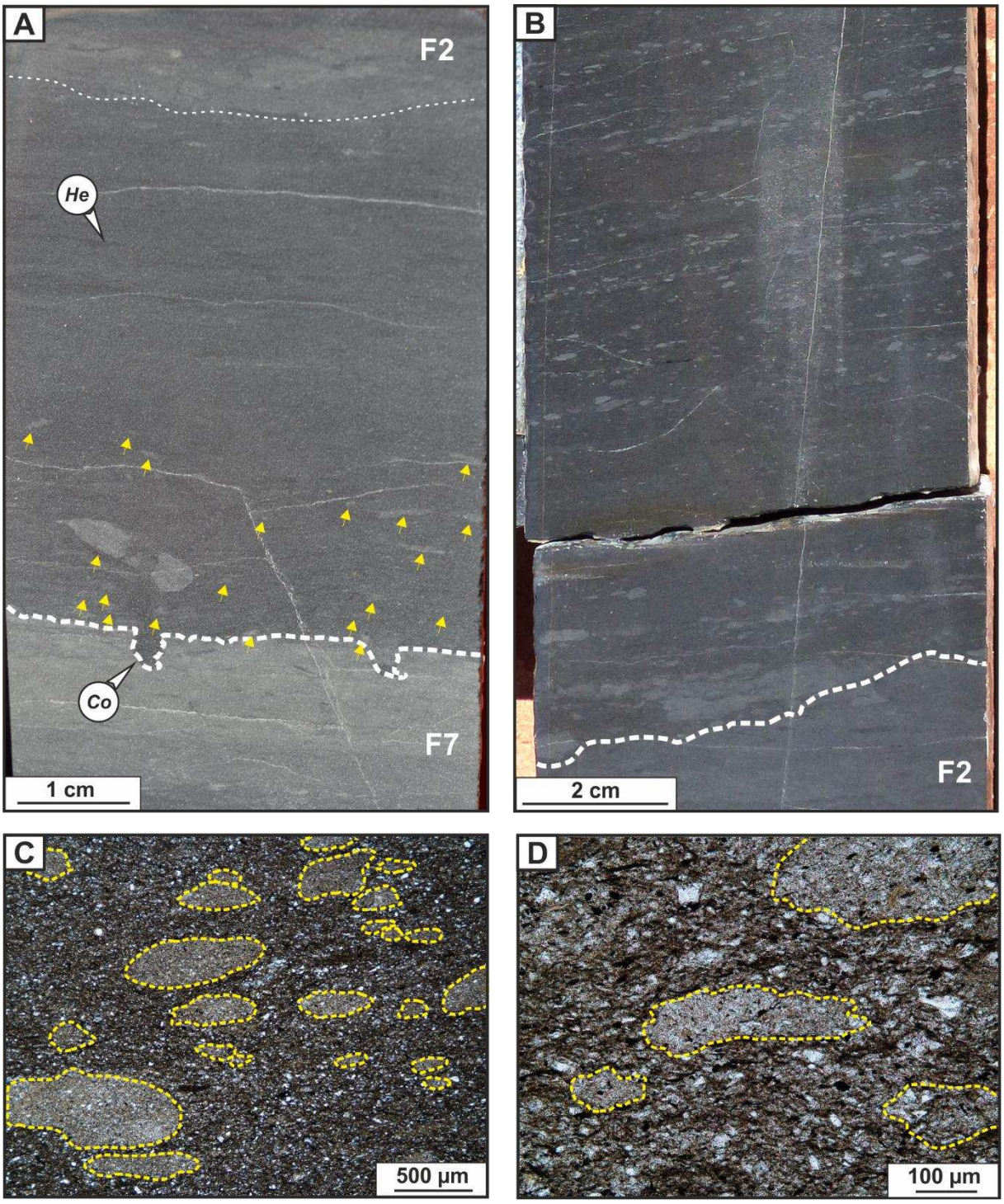

1188

1189 **Figure 6**

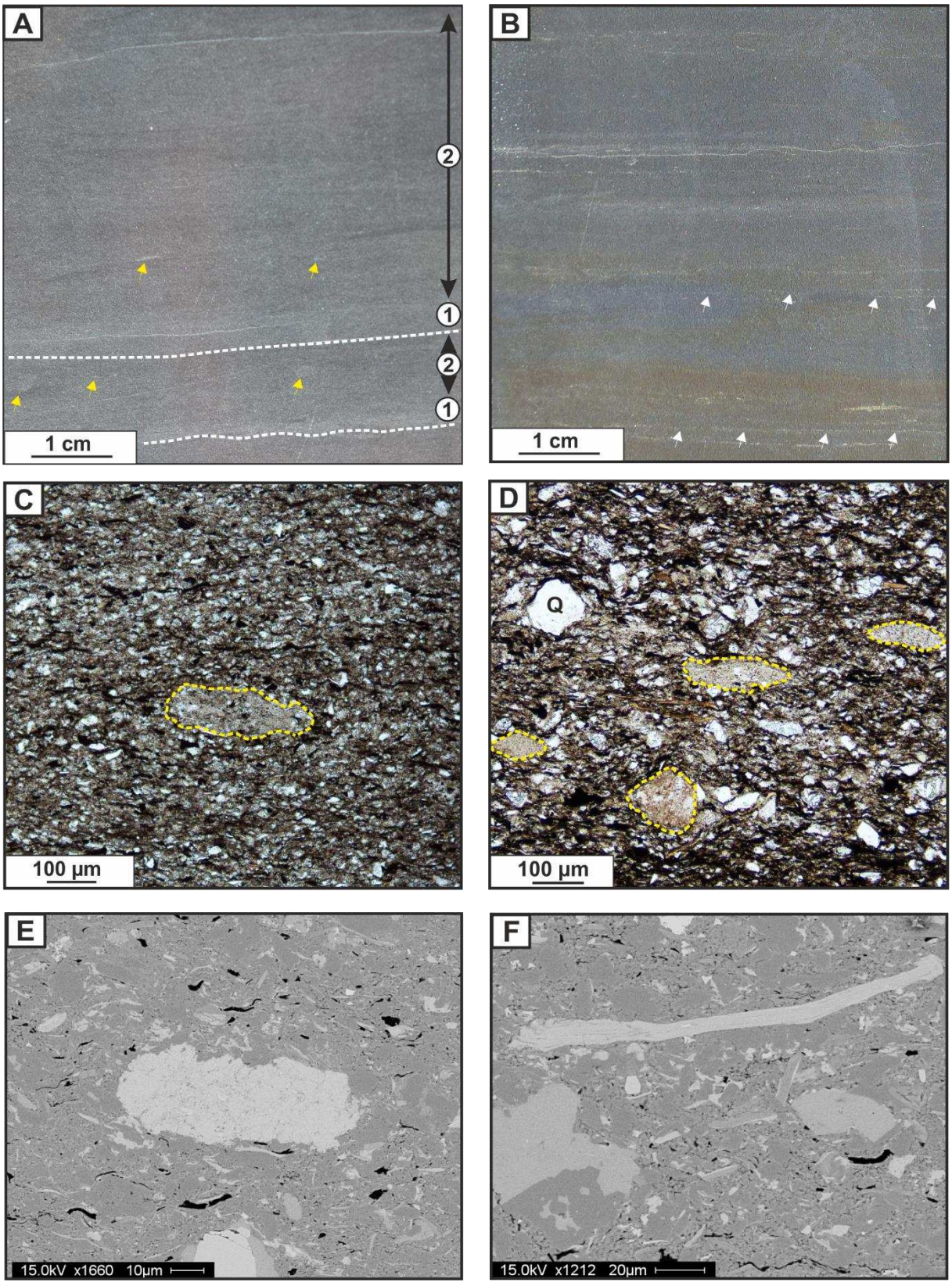
A
2
1
2
1
1 cm
B
1 cm
C
100 µm
D
Q
100 µm
E
15.0kV x1660 10µm
F
15.0kV x1212 20µm

Figure 7

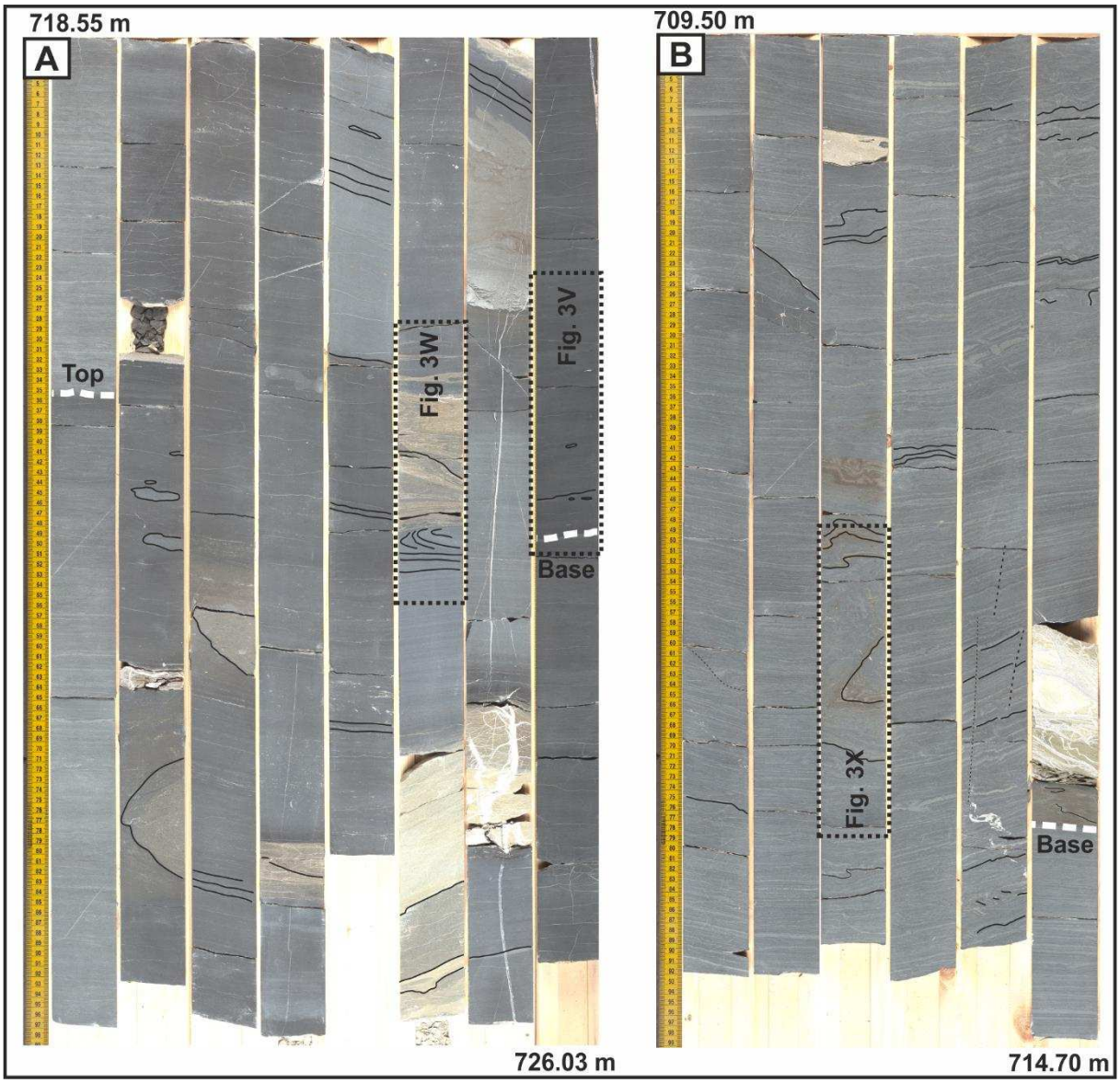

1192

1193 **Figure 8**

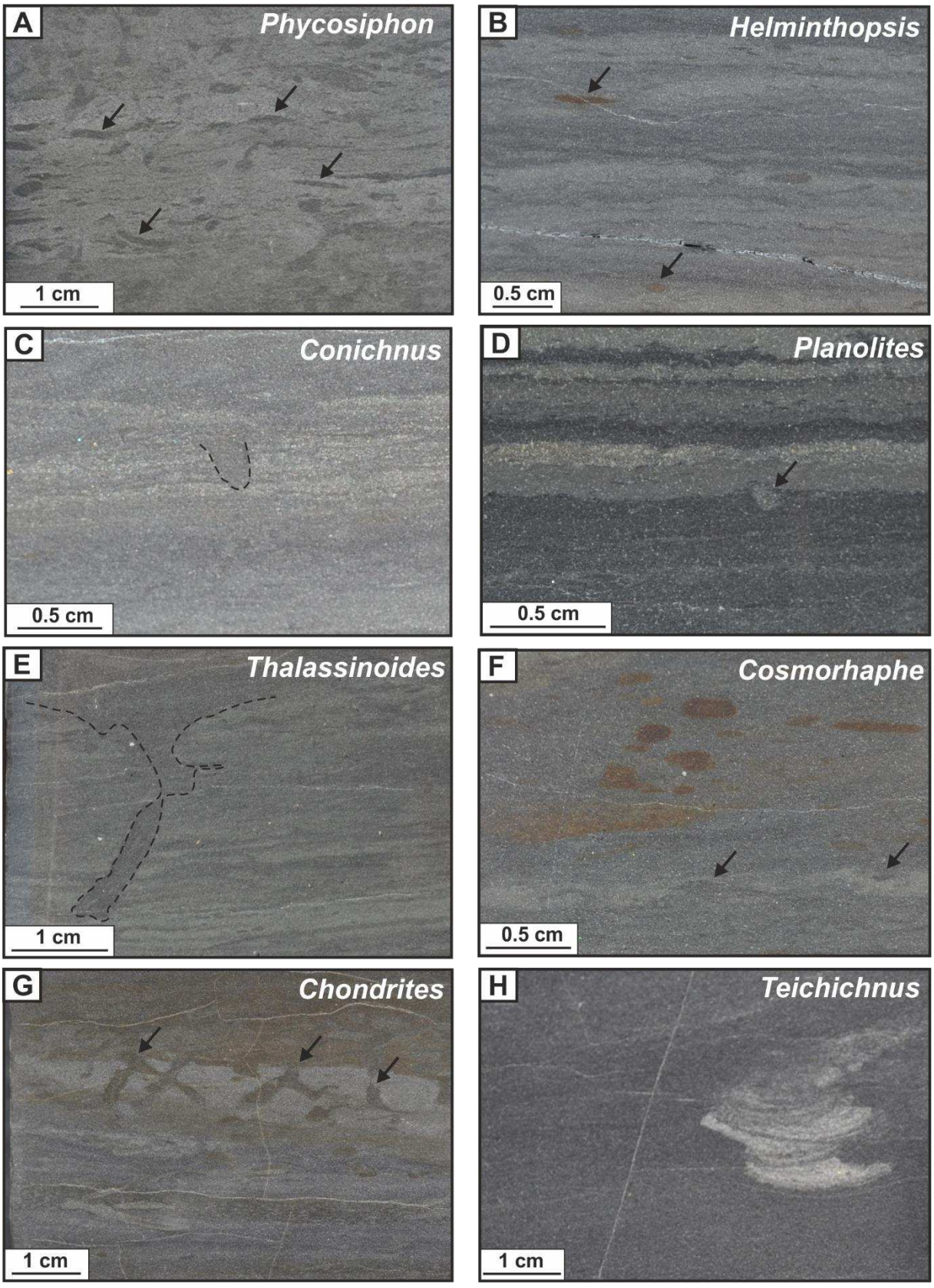

1194

1195 **Figure 9**

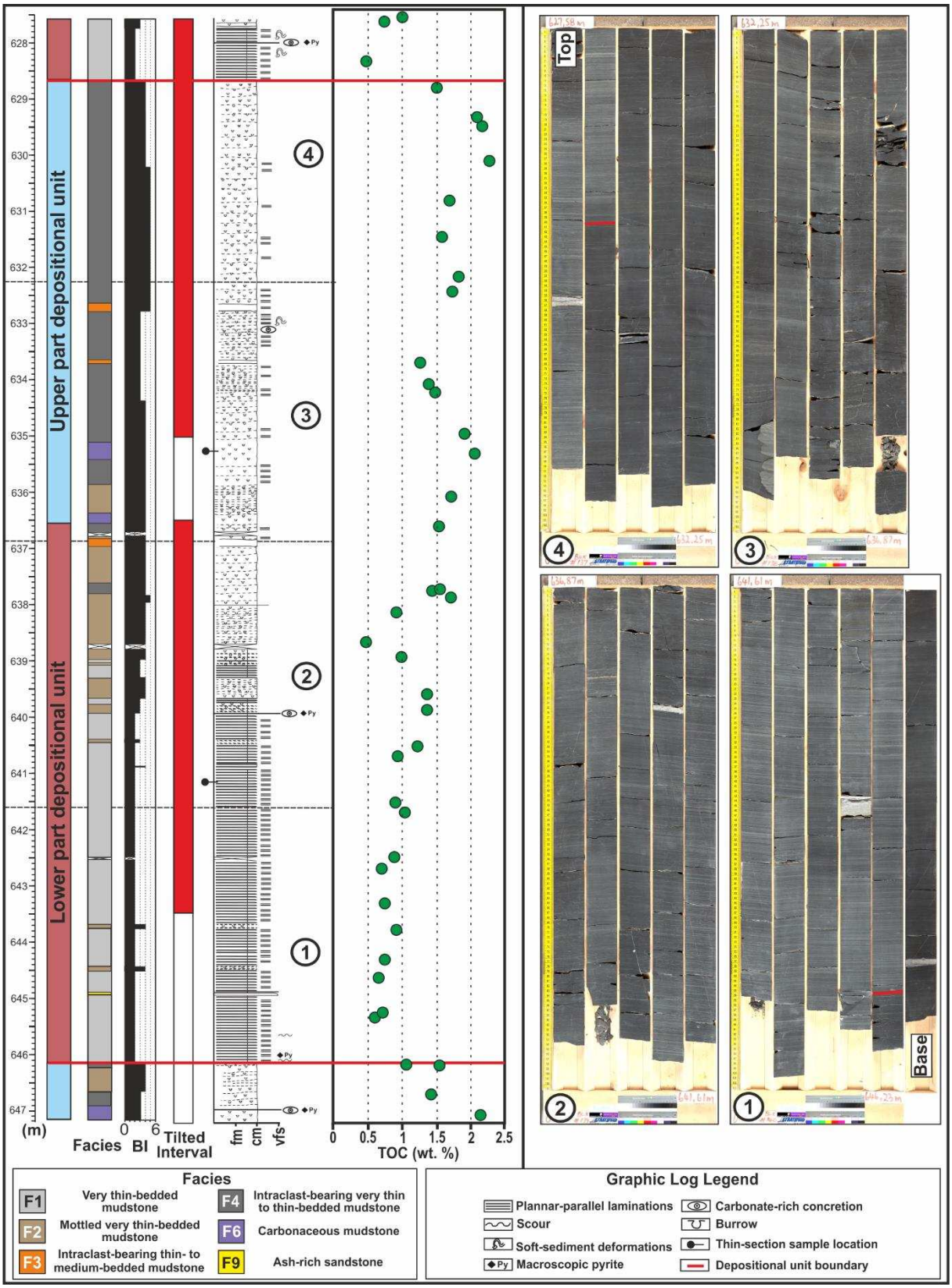

1196

1197 **Figure 10**

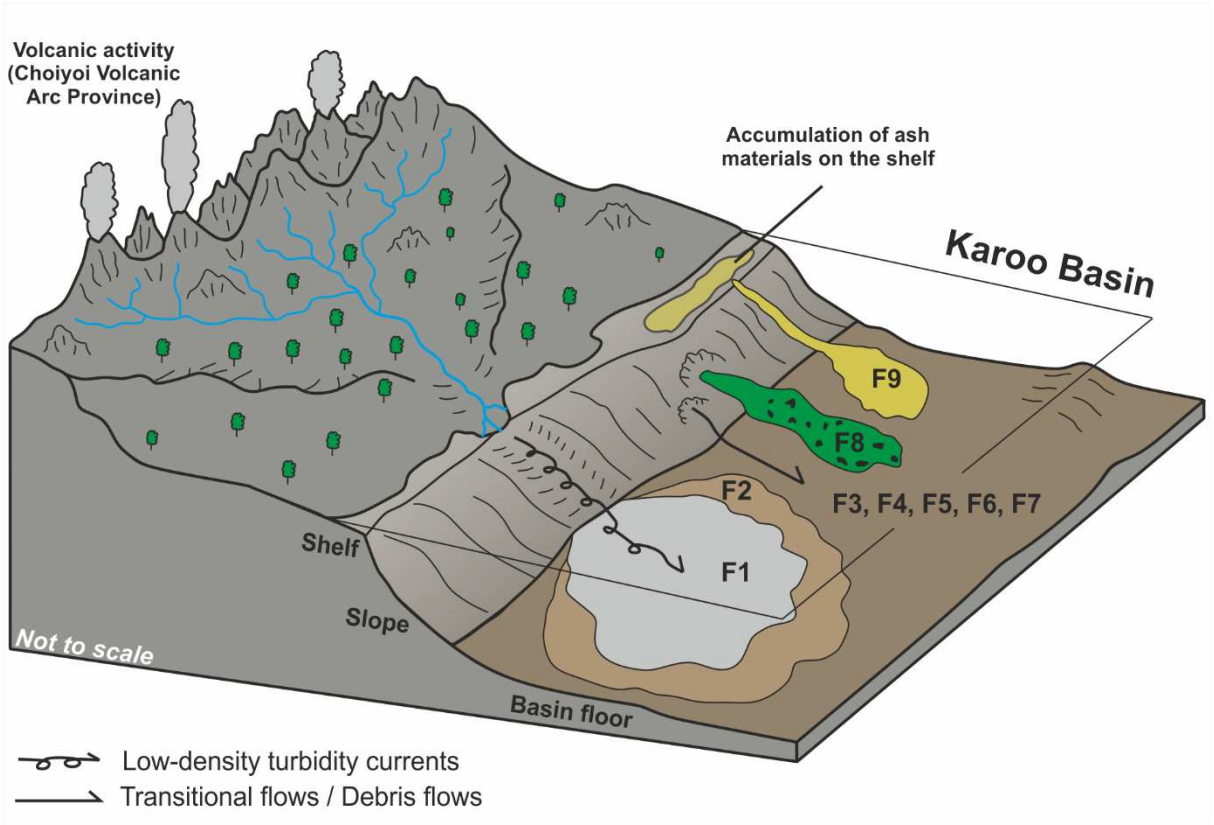

1198

1199 **Figure 11**

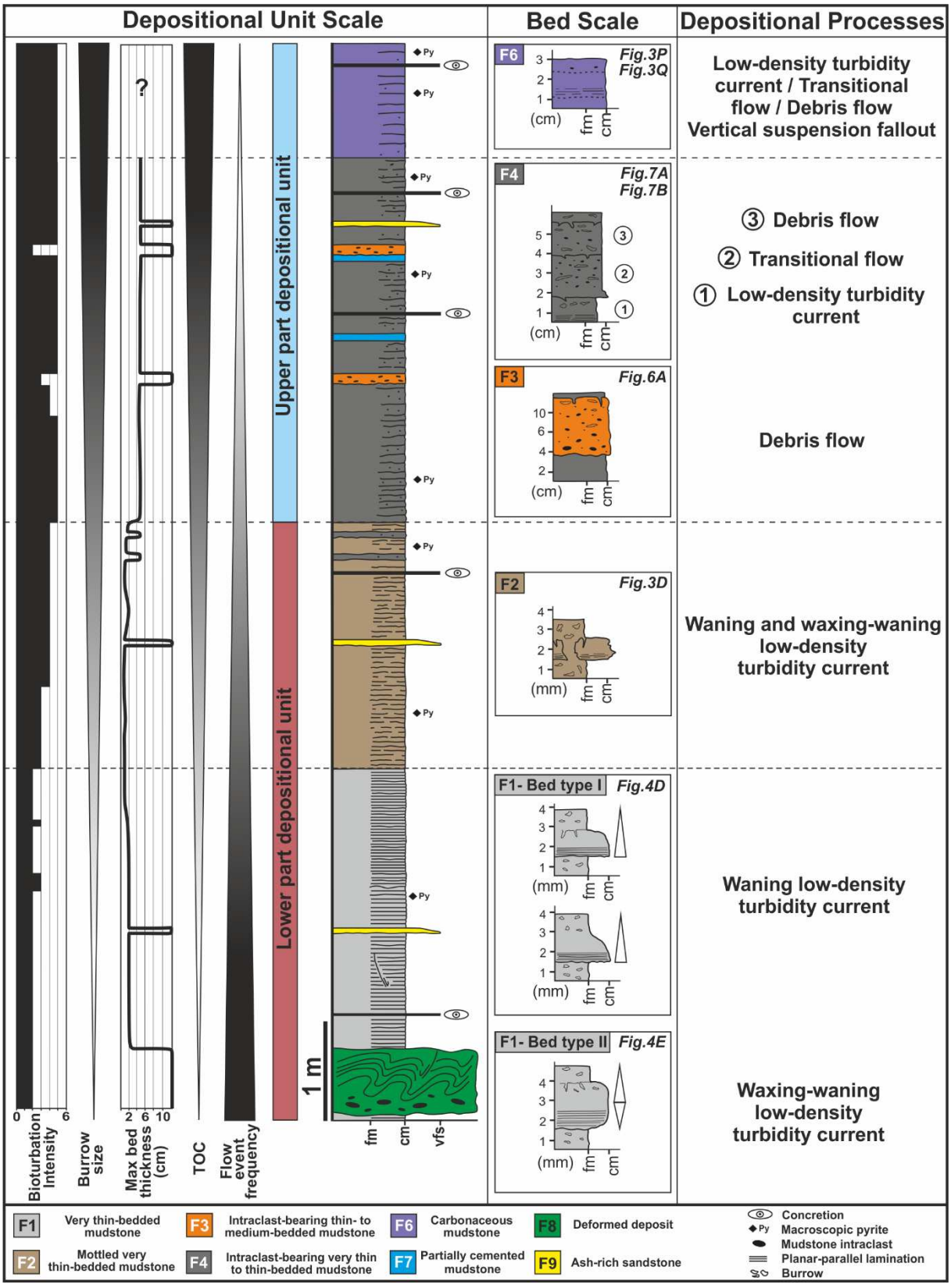
Depositional Unit Scale
Bed Scale
Depositional Processes
Upper part depositional unit
Lower part depositional unit
Bioturbation Intensity
Burrow size
Max bed thickness (cm)
TOC
Flow event frequency
1 m
fm
cm
vfs
F6
Fig.3P
Fig.3Q
Low-density turbidity current / Transitional flow / Debris flow
Vertical suspension fallout
F4
Fig.7A
Fig.7B
③ Debris flow
② Transitional flow
① Low-density turbidity current
F3
Fig.6A
Debris flow
F2
Fig.3D
Waning and waxing-waning low-density turbidity current
F1- Bed type I
Fig.4D
Waning low-density turbidity current
F1- Bed type II
Fig.4E
Waxing-waning low-density turbidity current
F1 Very thin-bedded mudstone
F2 Mottled very thin-bedded mudstone
F3 Intraclast-bearing thin- to medium-bedded mudstone
F4 Intraclast-bearing very thin to thin-bedded mudstone
F6 Carbonaceous mudstone
F7 Partially cemented mudstone
F8 Deformed deposit
F9 Ash-rich sandstone
Concretion
Py Macroscopic pyrite
Mudstone intraclast
Planar-parallel lamination
Burrow

Figure 12

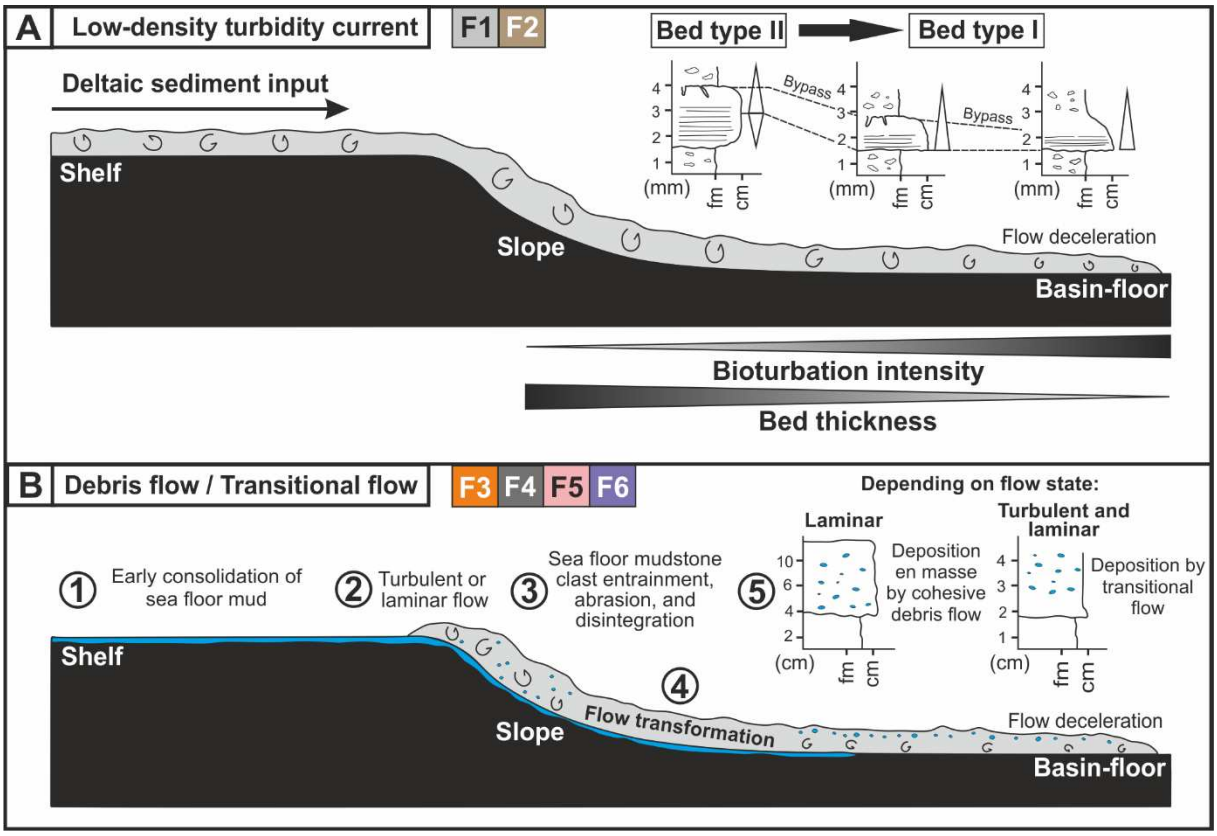

1202

1203 **Figure 13**